Dispersive fast magnetosonic waves and shock-driven compressible turbulence in the inner heliosheath

Bertalan Zieger[1], Merav Opher[1,2], Gábor Tóth[3], and Vladimir Florinski[4]

[1]Center for Space Physics, Boston University, Boston, MA, USA
[2]Astronomy Department, Boston University, Boston, MA, USA
[3]Department of Climate and Space Sciences and Engineering, University of Michigan, Ann Arbor, MI, USA
[4]Department of Space Science, University of Alabama, Huntsville, AL, USA

Key Points:

- Nonlinear dispersive fast magnetosonic waves produce 2-D compressible turbulence downstream of the termination shock.
- Taylor's hypothesis breaks down in the sub-fast-magnetosonic solar wind in the inner heliosheath.
- The magnetic turbulence spectrum observed by Voyager 2 in the inner heliosheath is reproduced by self-consistent three-fluid MHD simulation.

This is the author manuscript accepted for publication and has undergone full peer review but has not been through the copyediting, typesetting, pagination and proofreading process, which may lead to differences between this version and the Version of Record. Please cite this article as doi: 10.1029/2020JA028393

Corresponding author: Bertalan Zieger, berci@bu.edu

Abstract

The solar wind in the inner heliosheath beyond the termination shock (TS) is a non-equilibrium collisionless plasma consisting of thermal solar wind ions, suprathermal pickup ions and electrons. In such multi-ion plasma, two fast magnetosonic wave modes exist, the low-frequency fast mode and the high-frequency fast mode. Both fast modes are dispersive on fluid and ion scales, which results in nonlinear dispersive shock waves. We present high-resolution three-fluid simulations of the TS and the inner heliosheath up to a few AU downstream of the TS. We show that downstream propagating nonlinear fast magnetosonic waves grow until they steepen into shocklets, overturn, and start to propagate backward in the frame of the downstream propagating wave. The counter-propagating nonlinear waves result in 2-D fast magnetosonic turbulence, which is driven by the ion-ion hybrid resonance instability. Energy is transferred from small scales to large scales in the inverse cascade range and enstrophy is transferred from large scales to small scales in the direct cascade range. We validate our three-fluid simulations with in-situ high-resolution Voyager 2 magnetic field observations in the inner heliosheath. Our simulations reproduce the observed magnetic turbulence spectrum with a spectral slope of $-5/3$ in frequency domain. However, the fluid-scale turbulence spectrum is not a Kolmogorov spectrum in wave number domain because Taylors hypothesis breaks down in the inner heliosheath. The magnetic structure functions of the simulated and observed turbulence follow the Kolmogorov-Kraichnan scaling, which implies self-similarity.

1 Introduction

Multi-ion plasma, in general, contains more than one ion species (e.g. H^+ and He^{++}) or multiple ion populations with distinct physical characteristics, e.g. two ion populations with different bulk velocities (ion beams), or with different temperatures (non-equilibrium plasmas). The latter is common in magnetized collisionless space plasmas that include an ion source due to the ionization of a moving ambient neutral gas component. A typical example is the solar wind in the outer heliosphere, where a cold thermal ion population coexists with a hot suprathermal pickup ion (PUI) population. PUIs are created through charge exchange between solar wind protons and the neutral hydrogen component of the local interstellar medium and accelerated by the convection electric field of the solar wind. Other examples include the interaction region of the supersonic solar wind with cometary atmospheres, exospheres of weakly magnetized planets (Mars, Pluto), and the neutral hydrogen geocorona of Earth, or the interaction of planetary magnetospheric plasma with neutral sources from their moons (Io, Titan). It has remained largely unexplored how magnetosonic waves propagate and form shocks in such plasmas.

The Voyager spacecraft are the first man-made objects to cross the TS (Stone et al., 2005, 2008), where the solar wind becomes sub-fast-magnetosonic due to the interaction with the local interstellar medium. Voyager 2 observations revealed that classical single-fluid MHD or multi-species single-fluid MHD models (Isenberg, 1986; Whang, 1998; Usmanov & Goldstein, 2006; Usmanov et al., 2014; Zank et al., 2010; Zieger et al., 2013) (where the ion species and electrons are co-moving) are not sufficient to describe the observed nonlinear waves downstream the TS. Consequently, more sophisticated physical models, like multi-fluid MHD, hybrid or fully kinetic solar wind models are needed to capture nonlinear waves, dispersive shock waves and ion-ion instabilities, where each ion species (and electrons) can move independently with their own velocities, and the fluctuating parts of the ion velocities are often comparable to the mean velocity of the collective plasma fluid.

One important aspect to note is that by the very nature of PUIs (as they are picked up by the solar wind), they have the same average velocity as the thermal component: $\widetilde{\mathbf{u}}_{PUI} = \widetilde{\mathbf{u}}_{SW}$. However, the fluctuating parts ($\mathbf{u}''_{PUI}$ and $\mathbf{u}''_{SW}$) responsible for waves and turbulence can be different and quite large as non-linear structures develop, where

the ion velocities are decomposed to an average part and a fluctuating part as $\mathbf{u}_{PUI} = \widetilde{\mathbf{u}}_{PUI} + \mathbf{u}''_{PUI}$ and $\mathbf{u}_{SW} = \widetilde{\mathbf{u}}_{SW} + \mathbf{u}''_{SW}$. It is therefore necessary to solve the full multi-fluid equations with different momentum and energy equations for each ion species, unlike in multi-species single-fluid models, where only one momentum equation is solved for the collective fluid.

In multi-fluid MHD models of the solar wind (Zank et al., 2014; Zieger et al., 2015; Opher et al., 2020), suprathermal PUIs, thermal solar wind ions, and electrons are treated as three separate fluids with different ion velocities. Our multi-fluid MHD model was successful in reconstructing the nonlinear structure of the Voyager 2 TS crossing (Zieger et al., 2015). The addition of hot suprathermal ions to the mixture of thermal solar wind protons and electrons results in a high-frequency fast (HFF) mode and a low-frequency fast (LFF) mode, both of which are dispersive on fluid and ion scales. Positive dispersive wave modes can produce positive dispersive shock waves with a precursor wave train, and negative dispersive wave modes can produce negative dispersive shock waves with a trailing wave train (Biskamp, 1973; Hoefer, 2014). Dispersion is positive if the group velocity $\frac{\mathrm{d}\omega}{\mathrm{d}k}$ increases with increasing wave number, i.e. $\frac{\mathrm{d}^2\omega}{\mathrm{d}k^2} > 0$, and it is negative if the group velocity decreases with increasing wave number, i.e. $\frac{\mathrm{d}^2\omega}{\mathrm{d}k^2} < 0$. It was shown that the TS is a high-β low-Mach number (1.56) subcritical shock with a trailing wave train (Zieger et al., 2015), which is a negative dispersive shock wave in the LFF mode. Subcritical fast magnetosonic shocks are defined with the criterium $u_{n,2} < c_{s,2}$, i.e. the normal component of the downstream flow velocity is smaller than the downstream sound speed (Coroniti, 1970).

In case of subcritical high-β perpendicular shocks (where the fast Mach number is less than 2.76), kinetic effects such as ion reflection, shock surfing, and shock reformation can be neglected and the shock structure is controlled by dispersion (Edmiston & Kennel, 1984; Balogh & Treumann, 2013), which justifies the multi-fluid approach. However, in the high-β regime, the shock criticality strongly depends on the obliquity of the shock with the critical Mach number approaching one for parallel shocks. Using the properties of the trailing wave train downstream the TS, Zieger et al. (2015) were able to constrain the previously unknown PUI abundance and temperature. Their multi-fluid MHD simulations also confirmed the presence of a hot electron population at the TS, which has been predicted by a number of previous theoretical studies (Chalov & Fahr, 2013; Chashei & Fahr, 2014; Fahr et al., 2014). They showed that a significant part of the upstream kinetic energy of solar wind ions is transferred to the heating of PUIs and massless electrons, while the total hydrodynamic energy is conserved across the shock. A multi-fluid MHD model provides self-consistent energy partitioning across the TS, unlike the multi-species single-fluid models where additional assumptions are needed about the behavior of PUIs (Zank et al., 2010). In this paper, we present high-resolution three-fluid simulations of the TS and the inner heliosheath up to a few AU downstream of the TS. The three-fluid model produces self-consistent compressible turbulence in the inner heliosheath even with constant solar wind conditions upstream of the TS. We discuss the spectral properties and the spatial/temporal evolution of the turbulence and compare our results with in situ Voyager 2 observations in the inner heliosheath.

The paper is structured as follows. In Section 2, we briefly review the theory of dispersive magnetosonic waves and dispersive shock waves in collisionless plasma. In Section 3, we present our multi-fluid numerical simulation of compressible turbulence downstream of the TS and compare the simulation with the theoretical predictions. In Section 4, we validate the simulation results with in-situ Voyager 2 observations in the inner heliosheath. Conclusions are presented in Section 5.

2 Theory of Dispersive Fast Magnetosonic Waves in Non-equilibrium Collisionless Plasma

2.1 Dispersion Relation

The solar wind in the inner heliosheath beyond the TS is a non-equilibrium collisionless plasma consisting of thermal solar wind ions, suprathermal PUIs and electrons. Since the thermalization time scale is much larger than the convection time scale, and the convection time scale is much larger than the isotropization time scale of PUIs, the three-fluid description of the inner heliosheath plasma is a reasonable approximation. We use the standard set of multi-ion multi-fluid Hall MHD equations (Glocer et al., 2009; Zieger et al., 2015) to describe the three-fluid solar wind model with thermal solar wind ions (SW), PUIs, and electrons:

$$\frac{\partial \rho_j}{\partial t} + \nabla \cdot (\rho_j \mathbf{u}_j) = 0, \tag{1}$$

$$\frac{\partial (\rho_j \mathbf{u}_j)}{\partial t} + \nabla \cdot (\rho_j \mathbf{u}_j \mathbf{u}_j + p_j \tilde{\mathbf{I}}) = n_j q_j (\mathbf{u}_j - \mathbf{u}_+) \times \mathbf{B} + \frac{n_j q_j}{n_e e} (\mathbf{J} \times \mathbf{B} - \nabla p_e), \tag{2}$$

$$\frac{\partial \epsilon_j}{\partial t} + \nabla \cdot [(\epsilon_j + p_j)\mathbf{u}_j] = \mathbf{u}_j \cdot \left[n_j q_j (\mathbf{u}_j - \mathbf{u}_+) \times \mathbf{B} + \frac{n_j q_j}{n_e e} (\mathbf{J} \times \mathbf{B} - \nabla p_e) \right], \tag{3}$$

$$\frac{\partial \mathbf{B}}{\partial t} + \nabla \times (-\mathbf{u}_e \times \mathbf{B}) = 0, \tag{4}$$

$$\frac{\partial p_e}{\partial t} + \nabla \cdot (p_e \mathbf{u}_e) = -(\gamma - 1) p_e \nabla \cdot \mathbf{u}_e, \tag{5}$$

where ρ, n, q, $\mathbf{u}$ and p are mass density, number density, electric charge, velocity, and thermal pressure, respectively; index j stands for the two ion fluids (SW and PUI), and subscript e stands for the electron fluid; $\mathbf{B}$ is the magnetic field vector; $\mathbf{J} = \nabla \times \mathbf{B}/\mu_0$ is the current density; μ_0 is the permeability of free space; e is the elementary charge; $\gamma = 5/3$ is the adiabatic index; ϵ_j is the energy density of ion fluid j, defined as

$$\epsilon_j = \frac{\rho_j \mathbf{u}_j \mathbf{u}_j}{2} + \frac{p_j}{\gamma - 1}; \tag{6}$$

$\mathbf{u}_+$ is the charge averaged ion velocity, defined as

$$\mathbf{u}_+ = \frac{\sum_j n_j q_j \mathbf{u}_j}{\sum_j n_j q_j}; \tag{7}$$

and the electron velocity including the Hall term is

$$\mathbf{u}_e = -\frac{\mathbf{J}}{n_e e} + \mathbf{u}_+. \tag{8}$$

We solve separate continuity, momentum, and energy equations for each ion fluid, and close the set of multi-fluid MHD equations with the electron pressure equation. Heat conduction and viscosity is neglected in the collisionless solar wind plasma. Because of the relatively small characteristic length scale of our simulation (2 AU) we also neglect charge exchange, which plays otherwise an important role in global models of the inner heliosheath (Fahr et al., 2016; Scherer et al., 2018; Opher et al., 2020).

Linearizing the continuity and momentum equations (1) and (2), we can derive the following general dispersion relation of perpendicular magnetosonic waves in warm multi-fluid plasma (for the detailed derivation see Appendix B in Zieger et al. (2015)):

$$\left(\sum_j \frac{\omega_{pj}^2 \Omega_j}{\omega^2 - c_j^2 k^2 - \Omega_j^2}\right)^2 - \left(c^2 k^2 + \sum_j \frac{\omega_{pj}^2(\omega^2 - c_j^2 k^2)}{\omega^2 - c_j^2 k^2 - \Omega_j^2}\right)\left(\sum_j \frac{\omega_{pj}^2}{\omega^2 - c_j^2 k^2 - \Omega_j^2}\right) = 0, \quad (9)$$

where ω and k are the wave frequency and wave number, respectively, ω_{pj}, Ω_j, and c_j are the plasma frequency, the gyrofrequency and the sound speed of particle species j, and c is the speed of light. In case of three fluids, i.e. thermal solar wind ions, PUIs, and electrons, equation (9) reduces to a second order polynomial equation in ω^2, which can be solved analytically (Toida & Aota, 2013; Zieger et al., 2015).

There are two linear plane wave solutions: a low-frequency fast (LFF) mode and a high-frequency fast (HFF) mode. Thus, the multi-ion nature of the plasma creates two kinds of fast magnetosonic waves, a low-frequency mode that propagates mainly in the cold thermal population, and a high-frequency mode that propagates mainly in the hot PUI population. The HFF mode has a cutoff frequency (ω_{PUI0}) at the small wave number limit ($k \to 0$) that is independent of the plasma β defined as $\beta = 2\mu_0(p_{SW}+p_{PUI}+p_e)/B^2$:

$$\omega_{PUI0} = \left(\frac{\omega_{pSW}^2}{\Omega_{SW}^2} + \frac{\omega_{pPUI}^2}{\Omega_{PUI}^2}\right)\frac{\Omega_{SW}\Omega_{PUI}|\Omega_e|}{\omega_{pe}}. \quad (10)$$

The resonance frequency of the LFF mode is the ion-ion hybrid resonance frequency defined as

$$\omega_{SWr} = \left(\frac{\omega_{pSW}^2\Omega_{PUI}^2 + \omega_{pPUI}^2\Omega_{SW}^2}{\omega_{pSW}^2 + \omega_{pPUI}^2}\right)^{1/2}, \quad (11)$$

whereas the resonance frequency of the HFF mode is the lower-hybrid frequency defined as

$$\omega_{PUIr} = \left(\frac{\Omega_e^2}{\omega_{pe}^2}(\omega_{pSW}^2 + \omega_{pPUI}^2)\right)^{1/2}. \quad (12)$$

If both the solar wind ions and the PUIs are protons, Eq. (10) reduces to $\omega_{PUI0} = \Omega_H$, where Ω_H is the proton gyrofrequency, Eq. (11) reduces to $\omega_{SWr} = \Omega_H$, and Eq. (12) reduces to $\omega_{PUIr} = (\Omega_H\Omega_e)^{1/2}$.

In the cold plasma limit ($\beta = 0$), LFF waves in a two-ion-species plasma (e.g. H^+ and He^{++}) propagate in the frequency range between zero and the ion-ion hybrid resonance frequency, whereas HFF waves propagate in the frequency range between the cutoff frequency of the HFF mode and the lower hybrid frequency. There is a small frequency gap between the ion-ion hybrid resonance frequency and the cutoff frequency of the HFF mode, where linear magnetosonic waves cannot propagate. We are going to show that this is not true in the inner heliosheath, where the cold plasma approximation breaks down because β is of the order of 10 (Randol et al., 2013; Zieger et al., 2015; McComas et al., 2017).

In order to study the propagation of fast magnetosonic waves in the inner heliosheath on a theoretical basis, we calculated the multi-fluid linear dispersion relation, phase velocity, and group velocity of perpendicular fast magnetosonic waves downstream of the

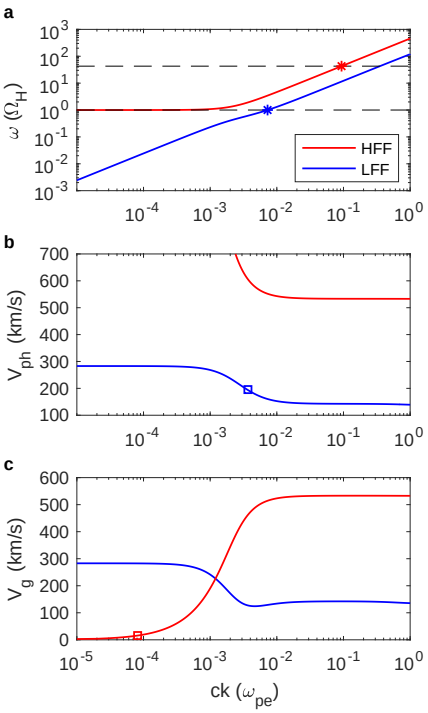

Figure 1. Characteristics of perpendicular fast magnetosonic waves downstream of the TS. (a) Dispersion relations of the high-frequency fast mode (HFF) or pickup ion mode and of the low-frequency fast mode (LFF) or solar wind ion mode. The cutoff frequency of the HFF mode and the resonance frequencies of the LFF and HFF modes are shown as dashed lines. The resonance points of the LFF and HFF modes are marked with asterisk symbols. (b) Phase velocities of the HFF mode and of the LFF mode. The blue square symbol marks the phase velocity and wave number of the quasi-stationary waves shown in Fig. 2b. (c) Group velocities of the HFF mode and of the LFF mode. The red square symbol marks the propagation velocity and wave number of the magnetic holes shown in Fig. 2c. The HFF mode is positive dispersive and the LFF mode is negative dispersive on fluid scales. The wave number is normalized to the reciprocal of the electron inertial length.

TS, which are shown in Fig. 1. Here the frequency is normalized to the proton gyrofrequency Ω_H, and the wave number is normalized to the reciprocal of the electron inertial length ω_{pe}/c. We used the downstream solar wind parameters for the third TS crossing (TS3) of Voyager 2 ($u_{SW,2} = 181.6$ km/s, $n_{SW,2} = 0.002375$ cm^{-3}, $T_{SW,2} = 0.2532$ MK, $B_2 = 0.1247$ nT, $n_{PUI,2} = 0.0005943$ cm^{-3}, $T_{PUI,2} = 20.34$ MK, $p_{e,2} = 0.05638$ pPa). These parameters are the mean downstream solutions of the best-fitting three-fluid model of the TS3 crossing in the hot electron case (Zieger et al., 2015). Similar mean downstream solutions were obtained for the extended shock simulation presented in Section 3.

As shown in Fig. 1a, the HFF mode has a cutoff frequency at the proton gyrofrequency (Ω_H), while the LFF mode can propagate at low frequencies without any frequency cutoff. The cutoff frequency of the HFF mode and the resonance frequencies of the LFF and HFF modes are marked with dashed lines in Fig. 1a. Note that the resonance frequency of the LFF mode ($\omega_{SWr} = \Omega_H$) coincides with the cutoff frequency of the HFF mode ($\omega_{PUI0} = \Omega_H$), and there is no frequency gap between the two. This implies that the HFF mode becomes unstable at the long wavelength (i.e. small wave number) limit ($k \to 0$) due to the ion-ion hybrid resonance instability of thermal solar wind ions and PUIs. The ion-ion hybrid resonance is expected to heat the solar wind plasma in the inner heliosheath. Unlike in case of cold plasma ($\beta = 0$), the frequencies of the LFF and the HFF waves do not approach the ion-ion resonance frequency and the lower hybrid frequency, respectively, at high wave numbers, but continue to increase with k above these resonance frequencies. Thus, the LFF and HFF modes become unstable at the wave number where their dispersion relation crosses the corresponding resonance frequency. The resonance points of the LFF and HFF modes are marked with blue and red asterisk symbols, respectively, in Fig. 1a. These resonance points predict narrow spectral peaks at the corresponding wave numbers in the turbulence spectra of the solar wind in the inner heliosheath. The ion-ion hybrid resonance instability in the LFF mode is predicted at the wave number of 0.00726 ω_{pe} (see blue asterisk in Fig. 1a).

In reality, the solar wind contains not only protons but also He^{++} ions (α particles) and other heavy ion species of very small abundance, and the PUIs are not purely interstellar H^+ (protons) but contain interstellar He^+ as well. Thus, multi-fluid theory predicts multiple narrow spectral peaks in the observed turbulence spectrum in the inner heliosheath, at the wave numbers of the ion-ion hybrid resonance instability of the H^+, He^{++}, and He^+ fast magnetosonic modes.

2.2 Dispersive Shock Waves and Shocklets

In single-ion plasma, magnetosonic waves become dispersive on the scale of the Debye length. However, in non-equilibrium plasma, like the solar wind that consist of thermal solar wind ions and hot PUIs, both fast magnetosonic wave modes are dispersive on ion scales and even on fluid scales. The HFF mode is positive dispersive because its group velocity increases with increasing wave number (see Fig. 1c). On the other hand, the LFF mode is negative dispersive on fluid scales because its group velocity is decreasing with increasing wave number. On ion scales, however, the LFF mode becomes positive dispersive at higher wave numbers (between 0.005 and 0.05 ω_{pe}), as shown in Fig. 1c.

Biskamp (1973) was among the first to suggest on the basis of theoretical considerations that subcritical shocks can produce a quasi-stationary trailing wave train downstream of the shock or a quasi-stationary precursor wave train upstream of the shock depending on the shape of the dispersion relation. If a linear dispersion relation bends upward (the group velocity increases) or downward (the group velocity decreases) at higher wave numbers, it will result in a precursor or trailing wave train, respectively. Thus, a subcritical shock in the negative dispersive LFF mode is expected to produce a trailing wave train, which has been confirmed by our numerical three-fluid simulation of the TS

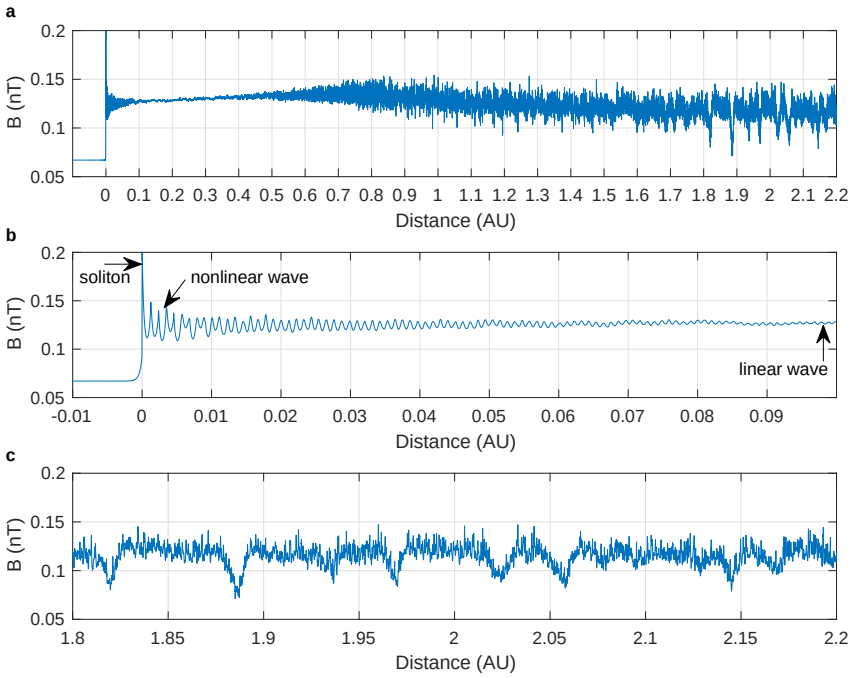

Figure 2. Three-fluid simulation of the TS and the turbulent inner heliosheath. (a) Magnetic field variations at and beyond the TS up to 2.2 AU downstream. (b) High-resolution section at the TS showing a coherent quasi-stationary dispersive shock wave with a soliton edge, a linear wave edge, and oscillatory nonlinear waves between the two (indicated by arrows). (c) High-resolution section in the inner heliosheath showing fully developed compressible turbulence with large-scale magnetic field depressions (magnetic holes).

(see Fig. 2b). More recently, Hoefer (2014) studied the long-term behavior of weak (small jump in density) dispersive shock wave solutions for dispersive Eulerian fluids without viscosity and heat conduction. It was shown that negative dispersive shock waves have a nonlinear trailing wave train downstream of the shock and positive dispersive shock waves have a nonlinear precursor wave train upstream of the shock. The dispersive shock wave has a stationary soliton edge (overshoot) at the shock front where the wave number approaches zero ($k \rightarrow 0$), and a linear wave edge downstream or upstream of the shock front, where the amplitude approaches zero. Interestingly, the velocity of the soliton edge is not the same as the velocity of the linear wave edge, which results in an expanding dispersive shock wave both in the negative and positive dispersion cases. In dispersive Eulerian fluids with zero viscosity and zero thermal conductivity, like a two-temperature collisionless plasma, weak shocks are characterized by an expanding oscillatory region with two speeds, in contrast to localized shock fronts propagating as travelling waves in classical, viscous fluids.

The overturning of downstream propagating compressional waves in collisionless dispersive plasma has been predicted by theory (Biskamp, 1973; McKenzie et al., 1993). For sufficiently small amplitudes, plane waves in a dispersive system can be described by the nonlinear Korteweg de Vries equation:

$$\frac{\partial u}{\partial t} + (u \pm c_s)\frac{\partial u}{\partial x} = a\frac{\partial^3 u}{\partial x^3}, \tag{13}$$

where u is the velocity amplitude, c_s is the sound speed, and the right-hand side term is the dispersion term, where a is the dispersion parameter. At the weak dispersion limit, the right-hand side becomes negligible. First, we consider an upstream propagating wave with a negative sign in Eq. (13). The wave becomes stationary ($\partial/\partial t = 0$) if $u = c_s$, which defines the sonic point. Now, we consider an upstream propagating wave with a positive sign in Eq. (13). Applying Galilean transformation to Eq. (13), we move to the frame that propagates with the sound speed in the downstream direction and find that the velocity is conserved ($\mathrm{d}u/\mathrm{d}t = 0$) at the weak dispersion limit ($a \rightarrow 0$). This means that a faster fluid element can overtake a slower fluid element ($\partial u/\partial x \rightarrow \infty$). The nonlinear steepening leads to a shocklet and eventually to the overturning of the wave. The solutions of the nonlinear Korteweg de Vries equation (Eq. (13)) for an upstream propagating disturbance are either periodic nonlinear waves or symmetric solitary waves (solitons). However, the soliton is transformed to an oscillatory shock wave if a small amount of dissipation is added (Biskamp, 1973).

In multi-ion plasma, the generalized sonic point is reached when the upstream propagating magnetosonic wave becomes stationary: $\partial u_j/\partial t = 0$. On the other hand, the critical locus is reached when the downstream propagating magnetosonic wave steepens into a shocklet and overturns in the frame propagating at the sound speed of the respective ion fluid (SW or PUI): $\mathrm{d}u_j/\mathrm{d}x \rightarrow \infty$. In multi-ion magnetized plasma, the generalized sonic point and the critical locus do not coincide (Dubinin et al., 2006). Thus, the nonlinear steepening of downstream propagating fast magnetosonic waves predicts both solar wind ion shocklets and PUI shocklets in the inner heliosheath that appear as thin current sheets or sudden jumps in the magnetic field intensity. The overturning of nonlinear fast magnetosonic waves results in counterpropagating waves, which is expected to drive strong compressible turbulence in the inner heliosheath even under steady upstream solar wind conditions.

2.3 Compressible Turbulence

Since the solar wind bulk flow velocity is mostly perpendicular to the ambient magnetic field in the inner heliosheath where Voyager 2 crossed the TS and the velocity perturbations of perpendicular fast magnetosonic waves are in the plane perpendicular to the ambient magnetic field, the magnetosonic turbulence in the inner heliosheath is ex-

pected to be 2-D compressible turbulence with no or negligible velocity perturbations in the parallel direction. What makes the difference between incompressible and compressible turbulence? The governing equations of incompressible turbulence are the conservation of mass, momentum, and magnetic flux, and the unknown variables are the velocity and magnetic field vectors and the plasma pressure. In the case of compressible turbulence, we have an additional equation for the conservation of energy and the equation of state, and there are two more unknown variables, the density and the energy.

In incompressible flows, we can decompose any variable Φ into a mean part ($\overline{\Phi}$) and a fluctuating part (Φ') using Reynolds averaging of the governing equations: $\Phi = \overline{\Phi} + \Phi'$, where $\overline{\Phi}$ is the average of Φ over time. The turbulent kinetic energy density is then defined as $\overline{u_i' u_i'}/2$, where u_i is the ith velocity component. However, this is not applicable in compressible flows because the density is not constant. In highly compressible flows, Favre averaging is needed to decompose some of the turbulent variable to $\Phi = \widetilde{\Phi} + \Phi''$, where $\widetilde{\Phi}$ is the density weighted average of Φ over time, i.e. $\widetilde{\Phi} = \overline{\rho\Phi}/\overline{\rho}$. In the compressible case, the turbulent kinetic energy density is defined as $\widetilde{u_i'' u_i''}/2$, i.e. $\overline{\rho u_i'' u_i''}/(2\overline{\rho})$ and the mean kinetic energy density is $\widetilde{u}_i \widetilde{u}_i/2$. In the averaged equations of compressible turbulence, Reynolds decomposition is used for the density, pressure, and magnetic field, and Favre decomposition is used for the velocity and the energy. Accordingly, we used Favre decomposition when calculating the turbulent kinetic energy spectra of solar wind ions and PUIs in Fig. 4. However, the difference between the Reynolds and Favre averaged mean ion velocities in the inner heliosheath is typically less than one percent, which is negligible. Thus, it would be sufficient to decompose all variables, including velocity and energy, with Reynolds averaging.

In incompressible 2-D plasma turbulence, the enstrophy is defined as the surface integral of the square of the vorticity

$$Z(\mathbf{u}) = \frac{1}{2}\int_S |\nabla \times \mathbf{u}|^2 dS. \tag{14}$$

In simple terms, it is related to the energy associated with the eddy motion of the plasma, and as such, it is conservative like the kinetic energy

$$E(\mathbf{u}) = \frac{1}{2}\int_S |\mathbf{u}|^2 dS, \tag{15}$$

as shown in turbulence theory (Kraichnan, 1967). More generally, when we are not restricted to incompressible flow, the enstrophy can be defined as the surface integral of the square of the Frobenius norm of the velocity gradient

$$Z(\mathbf{u}) = \frac{1}{2}\int_S ||\nabla \mathbf{u}||^2 dS. \tag{16}$$

The Frobenius norm of an $m \times n$ matrix $\mathbf{A}$ is defined as the square root of the sum of the absolute squares of its elements,

$$||\mathbf{A}|| = \sqrt{\sum_{i=1}^{m}\sum_{j=1}^{n} |a_{ij}|^2}. \tag{17}$$

In case of compressible magnetosonic turbulence in the inner heliosheath, we need to use Eq. (16) rather than Eq. (14) to calculate the enstrophy density spectra. Therefore, the enstrophy density spectra in Fig. 4 were calculated from the square of the Frobenius norm of the velocity gradient. Using energy conservation and enstrophy conservation arguments in stationary conditions, Kraichnan (1967) predicted a double cascade scenario in 2-D turbulence. If the turbulence is forced at intermediate scales, an inverse

energy cascade and a direct enstrophy cascade are expected to develop, where energy moves to large scales and enstrophy moves to small scales. So, the directions of the energy and enstrophy fluxes are opposite.

The non-stationary nature of the dispersive shock wave, i.e. the occasional steepening of nonlinear waves into shocklets, provides a constant source of magnetosonic perturbations in the downstream region. Downstream propagating linear LFF waves are expected to drive ion-ion hybrid resonance at the wavelength where the frequency of the linear waves matches the ion-ion hybrid resonance frequency (see Fig. 1a). The ion-ion hybrid resonance instability forces nonlinear magnetosonic waves at this intermediate scale. Since the velocity perturbations of perpendicular fast magnetosonic waves are 2-dimensional, Kraichnans theory (Kraichnan, 1967) predicts an inverse cascade of kinetic energy at large scales and a forward cascade of enstrophy at small scales in these downstream propagating waves. Overturning magnetosonic waves eventually result in forward and reverse shocklets that launch downstream (and upstream) propagating linear magnetosonic waves again further and further downstream and the development of the double cascade is repeated multiple times. This process is expected to create a fully developed stationary turbulent spectrum at wave numbers higher than the wave number of the overturning waves.

We are going to test and verify these theoretical predictions with numerical three-fluid simulation in Section 3.

3 Simulation of Fast Magnetosonic Turbulence in the Inner Heliosheath

3.1 Overturning of Fast Magnetosonic Waves

As demonstrated in the paper by Zieger et al. (2015), the multi-fluid 1-D simulation of the TS produces remarkable agreement with Voyager 2 observations, reproducing not only the microstructure of the TS3 crossing but also the energy partitioning among thermal ions, PUIs and electrons across the shock. In order to simulate the theoretically predicted overturning of downstream propagating fast magnetosonic waves in the inner heliosheath, we extended the grid of the 1-D simulation to 8 AU both upstream and downstream of the TS. We used the same upstream solar wind conditions as in the best fitting hot electron case in Zieger et al. (2015) ($u_{SW,1}$ = 320.7 km/s, $n_{SW,1}$ = 0.001278 cm^{-3}, $T_{SW,1}$ = 4155 K, B_1 = 0.06703 nT, $n_{PUI,1}$ = 0.0003195 cm^{-3}, $T_{PUI,1}$ = 13.42 MK, $p_{e,1}$ = 0.01833 pPa) for TS3 and the same grid resolution of 1000 km resolving the ion inertial length (4700 km) in the inner heliosheath. It was shown that the numerical solution was practically the same with a grid resolution of 500 km, which means that grid convergence had been achieved.

The initial left and right states are given by the upstream and downstream plasma parameters of the TS, where the downstream parameters are calculated from the generalized Rankine-Hugoniot jump conditions for the total fluid (the mixture of cold thermal ions, hot PUIs, and electrons). These boundary conditions result in a standing quasi-stationary shock solution in the inertial frame. The simulation was run for 20 days physical time to study the long-term behavior of the upstream propagating dispersive shock wave and the nonlinear growth and overturning of the downstream propagating LFF and HFF waves. We stopped the simulation before the fastest wave (HFF mode) had reached the outflow boundary at 8 AU downstream of the TS to avoid artificial reflection of waves from the boundary. A snapshot of the magnetic field variations at and beyond the TS up to 2.2 AU downstream is shown in Fig. 2a after 20 days of simulation in physical time. We show simulation results up to 2.2 AU because this is the distance that a solar wind parcel covers in 20 days in the inner heliosheath after crossing the TS. Although the different kinds of waves propagate much further downstream in the same time, the background solar wind parameters beyond 2.2 AU are not exact solutions of the three-fluid

model but they represent only the initial downstream conditions of the simulation. For this reason, we limited our analysis to the downstream region up to 2.2 AU.

Our three-fluid simulation shows that the dispersive effects of fast magnetosonic waves are manifested on the scale of astronomical units (AU), and dispersion plays a key role in the generation of compressible turbulence in the inner heliosheath. The quasi-stationary trailing wave train of the TS does not extend to infinity. Downstream propagating positive dispersive HFF (PUI mode) waves grow until they steepen into shocklets and eventually overturn starting to propagate backward in the frame moving downstream at the sound speed of the PUIs. Similarly, downstream propagating positive dispersive LFF waves (in the high wavenumber range of 0.005 to 0.05 ω_{pe}) grow nonlinearly until they steepen into shocklets and overturn as well. The counterpropagating fast magnetosonic waves (both LFF and HFF) produce fast magnetosonic turbulence in the heliosheath and limit the downstream extension of the quasi-stationary negative dispersive shock wave. Thus, our model produces coherent compressional waves in the post-shock region immediately downstream the TS (see Fig. 2b). Further downstream, nonlinear compressible turbulence develops in the inner heliosheath (see Fig. 2a) due to the nonlinear steepening and overturning of fast magnetosonic waves. The temporal evolution of turbulence eventually leads to large scale quasi-stationary structures like magnetic holes (see Fig 2c) and the turbulent kinetic energy is dissipated on large scales through solar wind heating and acceleration.

The negative dispersive shock wave in the magnetic field intensity shown in Fig. 2b is produced by upstream propagating negative dispersive nonlinear LFF mode waves. The overshoot at the shock front is the soliton edge predicted by the theory of dispersive shock waves (Biskamp, 1973). The smallest amplitude waves at 0.1 AU represent the linear wave edge of the negative dispersive shock wave, which moves downstream in time in the shock frame as predicted by theory (Hoefer, 2014). The oscillatory nonlinear waves appear quasi-stationary in the shock frame because the phase velocity of the wave is the same as the downstream flow velocity of the solar wind plasma. This has been verified by measuring the wavelength and phase velocity of the dispersive shock wave in the simulation. The blue square symbol in Fig. 1b marks the wave number and phase velocity obtained from the simulation. It lies exactly on the theoretical curve of the phase velocity of the LFF mode (blue line), implying a remarkable agreement between theory and the numerical three-fluid simulation. The nonlinear waves close to the soliton edge are non-sinusoidal and quasi-stationary in the sense that they can occasionally steepen into shocklets. The non-stationary nature of the dispersive shock wave provides a source of compressible disturbance that drives turbulence further downstream in the inner heliosheath.

The theoretically predicted expansion of the oscillatory region downstream of the TS has been confirmed by our 1-D three-fluid simulation. The linear wave edge of the negative dispersive shock wave reached 0.1 AU downstream of the TS in 66 hours. However, the linear wave edge eventually stopped moving downstream in the simulation. The dispersive shock wave became quasi-stationary in the shock frame after 82 hours and remained so until the end of the simulation at 22 days. This long-term behavior of the dispersive shock wave is probably due to the change in the sign of the dispersion of the LFF mode at higher wave numbers ($ck > 0.005\ \omega_{pe}$), as shown in Fig. 1c.

Our three-fluid MHD simulation confirms the theoretically predicted nonlinear steepening and overturning of downstream propagating perpendicular magnetosonic waves. The downstream propagating coherent LFF and HFF waves steepen into shocklets and start to propagate backward in the frame that propagates at the sound speed of the thermal solar wind ions or at the sound speed of the PUIs, respectively, which results in compressional turbulence further down in the inner heliosheath (see Fig. 2a and 2c). The overturning distance depends on the growth rate of the downstream propagating positive dispersive nonlinear HFF and LFF modes. In this particular simulation, the down-

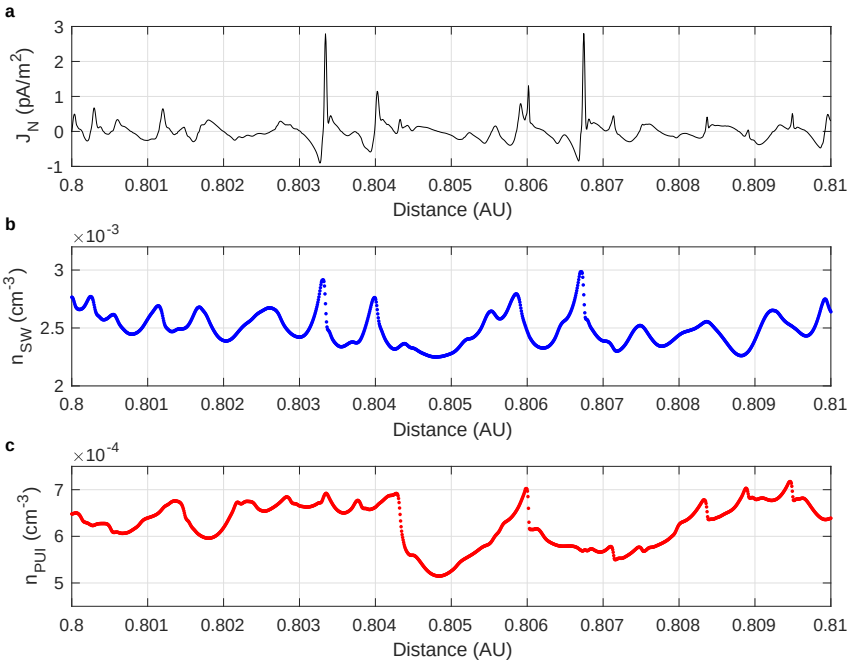

Figure 3. Nonlinear steepening of fast magnetosonic waves propagating downstream of the TS. (a) Thin current sheets associated with (b) forward shocklets in the solar wind ions (LFF mode) or (c) forward shocklets in the pickup ions (HFF mode). Since the two wave modes are independent, the occurrence of shocklets (sudden jumps or steep gradients in density) is not simultaneous in the solar wind ions and the pickup ions.

stream propagating nonlinear waves started to steepen into shocklets at around 0.8 AU downstream of the TS as shown in Fig. 3. Since the LFF (solar wind ion) and HFF (PUI) modes are independent, shocklets (sudden jumps) in the solar wind ion density (Fig. 3b) and in the PUI density (Fig. 3c) do not form simultaneously. However, both types of shocklets (LFF-mode and HFF-mode) appear as jumps in the magnetic field or peaks in the normal component of the current density (J_N), as shown in Fig. 3a. Although all the shocklets in Fig. 3 are forward shocklets, both forward and reverse shocklets occur further downstream in the turbulent inner heliosheath due to the overturning and counter-propagating fast magnetosonic waves.

As the turbulence develops in time in a downstream propagating fluid parcel, magnetic depressions or magnetic holes start to appear (see Fig. 2c). The physical process leading to the formation of these magnetic structures deserves more thorough theoretical discussion that is outside the scope of this paper. Nevertheless, one can easily find out which wave mode is responsible for these magnetic holes that have been observed by both Voyager 1 (Burlaga et al., 2007) and Voyager 2 (Burlaga et al., 2016). We can follow the same procedure that we used to identify the wave mode of the trailing wave train downstream of the TS crossing. Using two nearby time frames in the simulation, the propagation velocity of magnetic holes can be derived in the solar wind plasma frame by calculating a simple cross correlation function. Furthermore, we can also calculate the average wavelength of magnetic holes. We found that these magnetic holes are not frozen in the solar wind but are propagating at a very low speed (-15.7 km/s) in the upstream direction in the plasma frame. Since the solar wind speed (181.9 km/s at 2 AU downstream of the TS) is much higher than the propagation speed of magnetic holes, the magnetic holes are propagating downstream in the inertial frame. The velocity and

wave number of magnetic holes in the simulation defines a point (red square) in the group velocity plot of fast magnetosonic waves in Fig. 1c that lies exactly on the group velocity curve of the HFF mode. This implies that magnetic holes are most probably produced by HFF or PUI waves that propagate upstream at frequencies close to the ion-ion hybrid resonance frequency.

3.2 Double Cascade of Energy and Enstrophy

In order to study the temporal evolution of turbulence in a downstream propagating solar wind plasma parcel, we calculated the power spectra of different solar wind variables at increasing distances from the TS. Since downstream propagating fast magnetosonic waves are continuously generated by the TS, which is a quasi-stationary dispersive shock wave, a solar wind plasma element is exposed to magnetosonic perturbations the longer time, the further it has been carried downstream of the shock. Thus, the turbulence becomes more and more developed as we move further away from the TS.

First, we consider the spectral evolution of downstream propagating nonlinear fast magnetosonic waves before they overturn due to nonlinear steepening. As it is shown in Fig. 2a, the amplitude of coherent fast magnetosonic waves is gradually increasing between 0.2 and 0.8 AU until a maximum amplitude is reached around 0.8 AU. This is the point where downstream propagating LFF an HFF waves steepen into shocklets (see Fig. 3), overturn and start to propagate backward in the frame of the downstream propagating wave, which eventually leads to turbulence further downstream.

The evolution of the turbulent kinetic energy density spectra of solar wind ions and pickup ions between 0.2 and 0.8 AU are shown in Figs. 4a and 4b, respectively. Similarly, the evolution of the enstrophy density spectra of solar wind ions and PUIs are shown in Figs. 4c and 4d. The power spectra were calculated in a 0.4 AU sliding window with 0.2 AU stepping, which gives 50 percent data overlap between adjacent spectra. Each spectrum was produced with Welchs averaged periodogram method as follows. The 0.4 AU segment was divided into several smaller segments with 50% overlap. A modified periodogram was computed for each segment using a Hamming window and all the resulting Fourier spectra were averaged to compute the final power spectral density (PSD) estimate. This averaging method is to reduce the noise in the high-frequency part of the spectra.

The turbulent kinetic energy of solar wind ions and PUIs develop an inverse energy cascade in time where the energy moves toward large scales. This can be seen as a shift of spectral power toward larger and larger scales as the solar wind moves downstream from 0.2 AU to 0.8 AU. The arrows in Fig. 4a and Fig. 4b indicate the direction of the energy flux. On the other hand, the enstrophy of solar wind ions and PUIs develop a direct energy cascade in time, where enstrophy moves toward small scales. This is shown by the shift of spectral power to smaller and smaller scales as the solar wind moves downstream from 0.2 AU to 0.8 AU. The arrows in Fig. 4c and Fig. 4d indicate the direction of the enstrophy flux. This is consistent with the double cascade scenario in 2-D turbulence with steady forcing. The vertical dashed lines indicate the theoretically predicted wave number of ion-ion hybrid resonance instability of solar wind ions and PUIs, which divides the inverse and forward cascade ranges. This implies that the 2-D magnetosonic turbulence is forced by the ion-ion hybrid resonance instability. At 0.2 AU, the enstrophy density of solar wind ions has a large narrow peak at the wave number of the ion-ion hybrid resonance instability and other smaller peaks at its harmonics (see Fig. 4c), which confirms that the source of enstrophy is indeed the ion-ion hybrid resonance, where solar wind ions and PUIs collectively gyrate around each other. As the waves propagate downstream, enstrophy gradually moves to smaller scales. The turbulent kinetic energy of solar wind ions also has a strong initial peak at the wave number of the ion-ion hybrid resonance instability at 0.2 AU (see Fig. 4a). The highest nar-

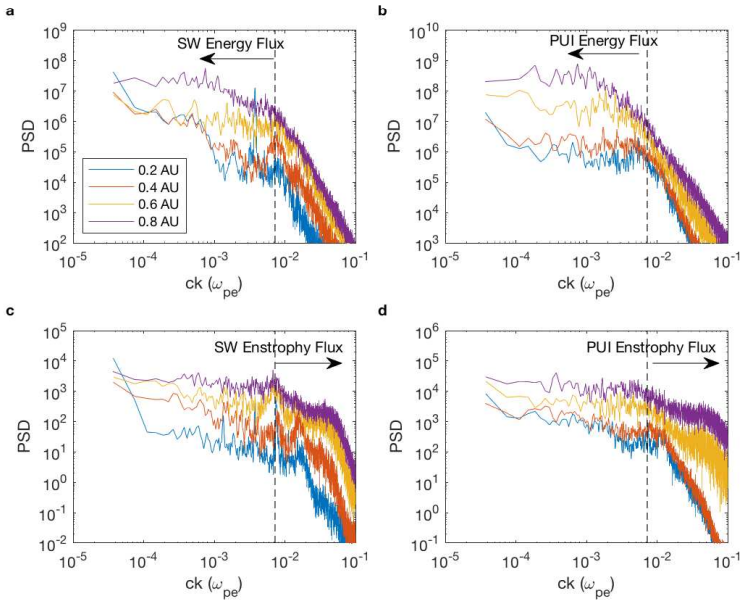

Figure 4. Inverse cascade of kinetic energy and direct cascade of enstrophy in fast magnetosonic waves propagating downstream in the plasma frame. (a) Kinetic energy density spectra of solar wind ions; (b) kinetic energy density spectra of pickup ions; (c) enstrophy density spectra of solar wind ions; and (d) enstrophy density spectra of pickup ions at different distances from the TS. Kinetic energy is transferred from small scales to large scales in the inverse cascade range and enstrophy is transferred from large scales to small scales in the direct cascade range. The vertical dashed line in each panel is the theoretically predicted wave number of the ion-ion hybrid resonance in the LFF mode (see blue asterisk in Fig. 1a).

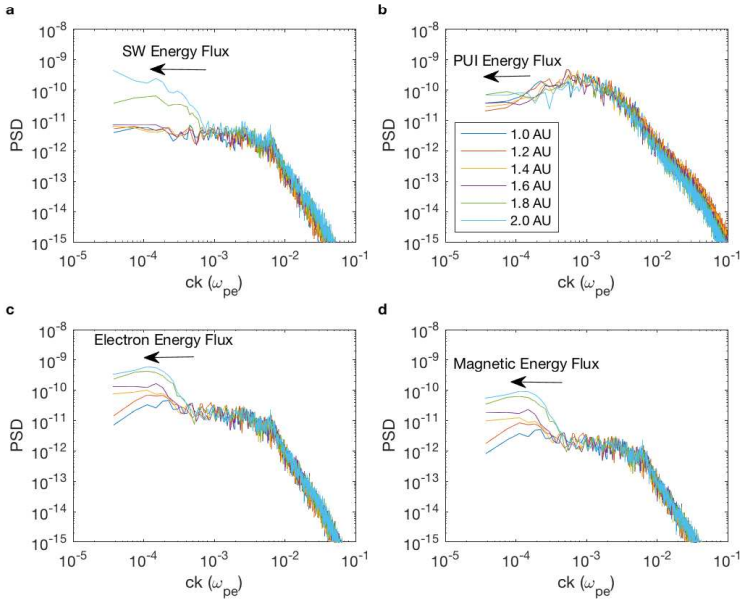

Figure 5. Inverse cascade of thermal energy in fast magnetosonic waves propagating upstream in the plasma frame. (a) Thermal energy density of solar wind ions; (b) thermal energy density of pickup ions; (c) thermal energy density of electrons; and (d) magnetic energy density at different distances from the TS. Thermal energy is transferred from small scales to large scales in the inner heliosheath.

row peak is produced not by downstream propagating waves but by the upstream propagating dispersive shock wave because the first 0.4 AU segment includes the TS as well. As the kinetic energy spectrum of downstream propagating waves evolve in time, energy gradually moves to larger scales until a quasi-steady spectrum is formed at 0.8 AU distance from the TS. At this point, a maximum power is reached in kinetic energy at the wave number where the downstream propagating waves overturn. The power of downstream propagating waves cannot grow further because they steepen into shocklets at this scale.

The evolution of the energy and enstrophy spectra of PUIs (see Figs. 4b and 4d) is very similar to that of the solar wind ions, showing a double cascade below and above the wave number of the ion-ion hybrid resonance instability. This means that not only the LFF mode but also the HFF mode is forced by the ion-ion hybrid resonance instability. A quasi-steady spectrum is formed at 0.8 AU in the PUI turbulent kinetic energy as well. However, the shapes of the energy spectra are different for thermal ions and PUIs, and the wave numbers of the maximum power are different, too. This is because the scales (wave numbers) where downstream propagating waves overturn are different for the LFF and HFF modes.

Next, we follow the evolution of the turbulent spectra of different solar wind variables in the turbulent region beyond 0.8 AU. Figure 5 shows the thermal energy spectra of solar wind ions, PUIs, and electrons as well as the magnetic energy spectrum at different distances from the TS. Overturning magnetosonic waves start to propagate in the opposite direction and the counterpropagating waves produce forward and reverse shocklets resulting in compressible fast magnetosonic turbulence. The randomly occurring reverse shocklets launch downstream propagating fast magnetosonic waves now and

again, maintaining a quasi-stationary energy and enstrophy flux at ion scales. As a result, a quasi-stationary turbulent spectrum develops in the inner heliosheath at large distances from the TS. Shocklets launch not only downstream propagating waves but also upstream propagating waves in the plasma frame. Upstream propagating magnetosonic waves contribute to the inverse energy cascade on fluid scales predicted by Kraichnans theory of 2-D turbulence. There is a constant flux of thermal energy towards large scales as indicated by arrows in Fig. 5. We verified that large-scale perturbations in the magnetic field, like magnetic holes in Fig. 2c, and the associated large-scale perturbations in density, pressure, and thermal energy propagate upstream in the plasma frame at the group velocity of the HFF mode (see Fig. 1c). This implies that the inverse energy cascade on fluid scale is mediated by upstream propagating HFF waves. The HFF mode approaches the frequency of the ion-ion hybrid resonance at large scales, which makes this wave mode unstable at the long wavelength limit. Since the group velocity of the HFF mode approaches zero at the long wavelength limit, the turbulent kinetic energy eventually dissipates on large scales in the form of solar wind heating and acceleration. The three-fluid simulation confirms the heating and acceleration of plasma as the turbulence develops in the downstream propagating solar wind. However, the discussion of solar wind heating and acceleration on the scales of astronomical units is outside the scope of this study.

3.3 Energy Spectra of Fully Developed Turbulence

We investigate the spectral properties of fully developed turbulence in our three-fluid simulation between 1.8 and 2.2 AU downstream of the TS. The magnetic field variations in this region are shown in Fig. 2c. The goal of this analysis is to understand the spectral shapes of different turbulent variables, like velocity, density, pressure, energy, and magnetic field. Why are they different or why are they similar? Where do spectral breaks occur and what is their physical explanation? What can we learn about fast magnetosonic turbulence in the heliosheath if only magnetic observations were available?

The hydrodynamic energy spectra of solar wind ions and PUIs are shown in Fig. 6a and Fig. 6b, respectively. The spectral slopes are significantly different and the shape of the spectra are very different as well. This is attributed to the differences in the dispersion relations of the two fast magnetosonic modes. The spectral break in the hydrodynamic energy spectrum of solar wind ions in Fig. 6a is at higher wave number ($\sim 4.7\times10^{-3}$ ω_{pe}) than the corresponding spectral break in the hydrodynamic energy spectrum of PUIs in Fig. 6b ($\sim 1.8\times10^{-3}$ ω_{pe}). These spectral breaks appear at the wave number where the downstream propagating nonlinear LFF and HFF waves steepen into shocklets and overturn. This is where the downstream propagating LFF and HFF waves reach their large-scale dissipation range above the intermediate-scale production range where the turbulence is forced by the ion-ion hybrid resonance instability (at the wave number of 7.3×10^{-3} ω_{pe}).

The spectral break in the hydrodynamic energy spectrum of solar wind ions coincides with the wavenumber where the group velocity of LFF waves has a local minimum (see Fig. 1c), i.e. where $\mathrm{d}^2\omega_{SW}/\mathrm{d}k^2$ changes sign. LFF waves above the spectral break are positive dispersive and propagate downstream, while LFF waves below the spectral break are negative dispersive and propagate upstream in the frame of the downstream propagating wave. The spectral break in the hydrodynamic energy spectrum of PUIs coincides with the wave number where the second derivative of the group velocity of HFF waves has a local minimum, i.e. where $\mathrm{d}^4\omega_{PUI}/\mathrm{d}k^4$) changes sign. Thus, the dissipation scales of LFF and HFF waves in inviscid collisionless plasma are determined by the shape of their dispersion relation not by the parameters of viscosity and large-scale friction, as in 2-D incompressible fluid turbulence (Kraichnan, 1967). Dissipation downstream of subcritical collisionless shocks are controlled by dispersion.

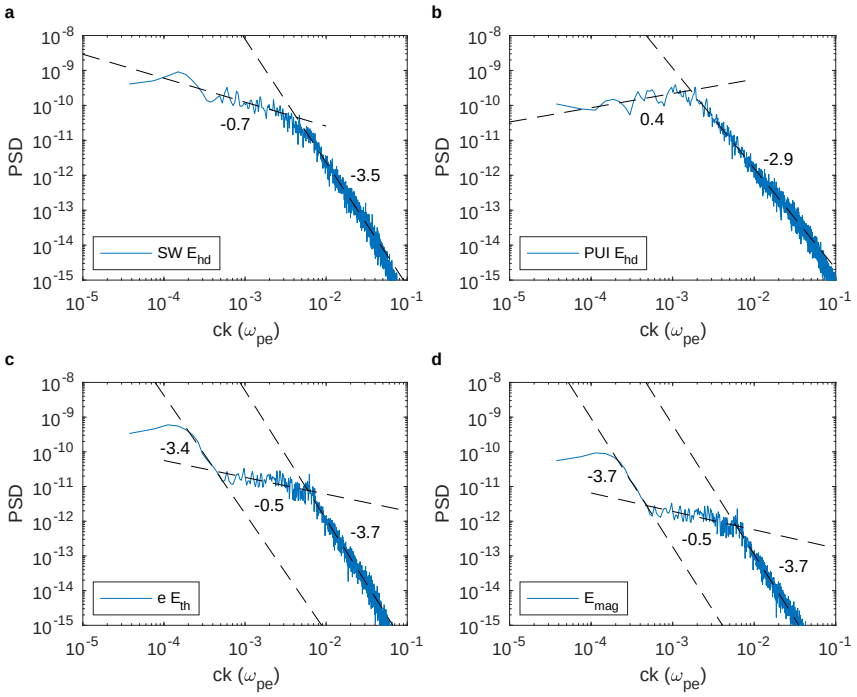

Figure 6. Energy spectra of fully developed magnetosonic turbulence in the inner heliosheath between 1.8 and 2.2 AU downstream of the TS. (a) Hydrodynamic energy spectrum of solar wind ions; (b) hydrodynamic energy spectrum of pickup ions; (c) thermal energy spectrum of electrons; and (d) magnetic energy spectrum. The best fitting spectral slopes are plotted as dashed lines and marked with the corresponding scaling exponents.

The scaling exponents of the hydrodynamic energy spectra in the production range where the turbulence is forced are -3.5 and -2.9 for solar wind ions and PUIs, respectively. In the range where the LFF and HFF waves overturn and propagate in the opposite direction, the scaling exponents of the hydrodynamic energy spectra are -0.7 for thermal ions and 0.4 for PUIs. The opposite spectral slopes can be explained with the sign of dispersion of overturning LFF and HFF waves. Overturning LFF waves become negative dispersive, while overturning HFF waves remain positive dispersive. Thus, upstream propagating LFF waves are amplified and upstream propagating HFF waves are damped. However, damped HFF waves can still propagate because of the constant energy flux of the inverse cascade.

The hydrodynamic energy spectrum of electrons is practically identical with the thermal energy spectrum of electrons (Fig. 6c) because of the negligible kinetic energy of electrons due to the low electron mass. It is very similar to the magnetic energy spectrum in Fig. 6d. This similarity is not unexpected as in the multi-fluid model the magnetic field is frozen in the electron fluid (see Eq. (4)). For the same reason, the power spectrum of the electron density (or the total ion density) and the power spectrum of the magnetic field are expected to be very similar, too. Unlike in case of the hydrodynamic energy spectra of ions, the spectral break in the magnetic and electron energy spectra at intermediate scales coincides with the wave number of the ion-ion hybrid resonance instability ($7.3\times10^{-3}\ \omega_{pe}$). The second spectral break at the wave number of $\sim4.5\times10^{-4}$ ω_{pe} on fluid scale coincides with the wave number where the frequency of HFF waves approach the ion-ion hybrid resonance frequency, i.e. $\omega_{PUI} \rightarrow \Omega_H$ (see Fig. 1a). The inverse cascade of thermal energy (see Fig. 5) and the inverse cascade of magnetic energy on fluid scales is therefore driven by HFF mode waves with frequencies approaching the proton gyrofrequency. The spectral slope of the inverse cascade on fluid scale is comparable to the spectral slope of the direct cascade on ion scale, both having a scaling exponent close to -3.7 (see Figs. 6c and and. 6d). The inverse energy cascade on fluid scale is expected to extend to even larger scales as the turbulence develops in time, but our multi-fluid simulation was limited to 20 days physical time only. As demonstrated in Fig. 6, the hydrodynamic energy spectra of thermal ions and PUIs are controlled by the dispersion of the LFF and HFF modes and do not reveal where the turbulence is forced. In contrast, the magnetic energy spectrum reveals the scale where the turbulence is forced but does not show the dissipation ranges of the HFF and LFF waves where the downstream propagating waves overturn.

In the next section, we are going to validate our three-fluid simulation of magnetosonic turbulence with high-resolution (48 s) magnetic field observation in the inner heliosheath by the Voyager 2 spacecraft.

4 Model Validation with Voyager 2 Observations

4.1 Reconstruction of the Voyager 2 Termination Shock Crossing

Voyager 2 crossed the TS multiple times on August 31 and September 1, 2007 at 83.7 AU from the Sun (Burlaga et al., 2008). The multiple crossings imply that the TS was not stationary but moved toward and away from the Sun due to varying upstream solar wind conditions. The compression ratios at the second (TS2) and third crossings (TS3) were in the range $2.1-2.4$ and $1.6-1.8$, respectively (Richardson et al., 2008; Zieger et al., 2015). Both TS2 and TS3 were subcritical perpendicular shocks with fast magnetosonic Mach numbers of 1.56 and 1.93, respectively. However, the upstream conditions at TS2 were more variable due to upstream solar wind turbulence. The microstructure of TS3 was successfully reconstructed by multi-fluid (Zieger et al., 2015) and particle-in-cell simulations (Yang et al., 2015). These simulations revealed a quasi-stationary shock structure with a ramp, an overshoot and an oscillatory wave train downstream of the shock front. The simulation of Yang et al. (2015) showed that the addition of 25% PUIs sig-

nificantly reduced ion reflection from the shock. However, the shock front remained non-stationary exhibiting a rippled structure. Zieger et al. (2015) found that the multi-fluid simulation with 20% PUIs provided the best fit to Voyager 2 observations and concluded that the TS is a high-β low-Mach number subcritical dispersive shock wave. Voyager 2 observed strong compressible magnetic field variations in the 48-second magnetic data downstream the TS at the end of 2007 and in the beginning of 2008 (Burlaga & Ness, 2009). These compressible variations included large-amplitude coherent structures in the post-shock region and weaker more random magnetic field variations in a unipolar region further downstream. The distribution of magnetic field increments was shown to be non-Gaussian on different scales from 48 s to several hours in both regions.

The large amplitude coherent magnetosonic waves observed in the post-shock region are consistent with the prediction of a coherent nonlinear dispersive shock wave downstream of the TS as shown in Fig. 2b. Note that the upstream conditions were kept constant for 20 days in our simulation, which allowed the long-term temporal evolution of the dispersive shock wave. In reality, upstream conditions at the TS changed more rapidly, on the time scale of days or less, which limited the coherence length scale of dispersive shock waves. Consequently, the downstream region is expected to be a superposition of several dispersive shock waves with intermittent random variations.

4.2 Breaking Down of Taylors Hypothesis

In order to allow direct comparison between the multi-fluid simulation and the high-resolution magnetic field observations of Voyager 2 in the inner heliosheath, we flew a virtual satellite in our time-dependent simulation across the turbulent downstream region at the speed of the Voyager 2 spacecraft and sampled the MHD variables in time domain. Then we calculated 48-sec averages of the magnetic field and plasma variables to produce a simulated Voyager 2 time series that could be directly compared with actual data.

First, we wanted to test the validity of Taylors hypothesis in the heliosheath, which assumes that the observed temporal variations in the spacecraft frame correspond to spatial variations in the plasma frame. This is generally thought to be valid in the supersonic solar wind due to the large velocity difference between the spacecraft and the solar wind but not necessarily valid in the heliosheath behind the TS where the fast magnetosonic speed exceeds the downstream flow velocity. The relationship between wave frequencies observed in the spacecraft frame (f_{SC}) and in the plasma frame (f_{PL}) can be described with the Doppler shift equation:

$$f_{SC} = f_{PL} + \frac{1}{2\pi}\mathbf{k}\cdot\mathbf{v}_{rel}, \tag{18}$$

where $\mathbf{k}$ is the wave number vector and $\mathbf{v}_{rel}$ is the relative velocity between the solar wind and the spacecraft. Taylors hypothesis (Taylor, 1938) requires that

$$f_{PL} \ll \frac{1}{2\pi}\mathbf{k}\cdot\mathbf{v}_{rel}, \tag{19}$$

which means that the phase velocity of waves in the direction of the relative velocity is much smaller than the relative speed between the spacecraft and the solar wind ($v_{ph} = \omega/k \ll \mathbf{v}_{rel}$). Since the solar wind flow and the direction of motion of Voyager 2 is radially outward at the TS and the magnetic field is predominantly in the azimuthal direction, Taylors hypothesis should be considered for the fastest wave mode in the perpendicular direction, which is the HFF mode. As shown in Fig. 1b, the phase velocity of the perpendicular HFF mode is much larger than the downstream flow velocity of 182 km/s especially at large scales where the phase velocity exceeds 10^4 km/s. The phase velocity of the LFF mode is also larger than the downstream flow velocity (indicated by

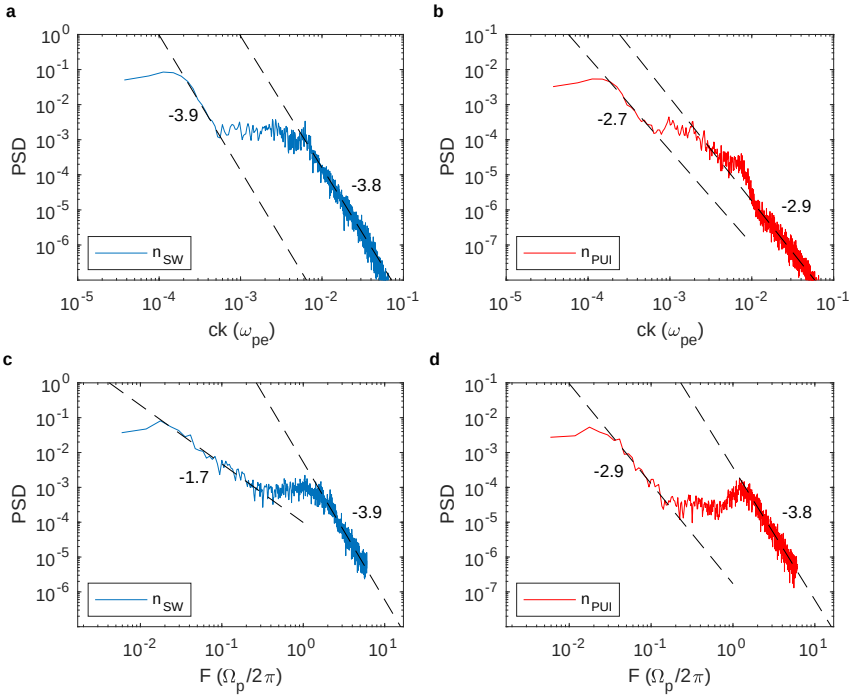

Figure 7. Breaking down of Taylors hypothesis in the inner heliosheath. (a) Power spectrum of solar wind ion density in wave number domain; (b) power spectrum of pickup ion density in wave number domain; (c) power spectrum of solar wind ion density in frequency domain; and (d) power spectrum of pickup ion density in frequency domain as it would be observed by the Voyager 2 spacecraft between 1.8 and 2.2 AU downstream of the TS. The best fitting spectral slopes are plotted as dashed lines and marked with the corresponding scaling exponents. Since the density spectra are very different in the wave number and frequency domains for both solar wind ions and pickup ions, Taylors hypothesis of observing predominantly spatial variations by a spacecraft in frequency domain apparently breaks down in the sub-fast-magnetosonic inner heliosheath.

a blue square) on fluid scales, but it becomes smaller than that on ion and electron scales. Thus, Taylors hypothesis clearly breaks down for fast magnetosonic turbulence.

In order to demonstrate the breaking down of Taylors hypothesis in the inner heliosheath, we computed the turbulent spectra of solar wind ion density and PUI density both in wavenumber and frequency domains using the time series of the virtual spacecraft moving at the speed of Voyager 2 in the multi-fluid simulation. In Fig. 7, we adjusted the frequency range to the wave number range with the linear conversion formula of Eq. (18), assuming that Taylors hypothesis was true. The spectra in wave number and frequency domains should be identical if Taylors hypothesis was true. This is apparently not the case. The spectral shapes and the spectral slopes in Fig. 7 are significantly different in the wave number and frequency domains both for solar wind ions and PUIs. This means that Taylors hypothesis generally breaks down for both the LFF and HFF waves in the inner heliosheath. Although the density spectrum of solar wind ions looks like a Kolmogorov spectrum in frequency domain having a scaling exponent close to $-5/3$ on fluid scales, the actual scaling exponent is not -1.7 but -3.9 in wave number domain. This means that the turbulent spectrum of fast magnetosonic waves cannot be determined with a single spacecraft flying at the speed of Voyager 2. Only multi-spacecraft obser-

vations could distinguish between spatial and temporal variations in the inner heliosheath. Note that the spectral shape of solar wind ion density in Fig. 7a and the spectral shapes of electron thermal energy and magnetic energy densities in Figs. 6c and 6d are very similar. This can be understood as a consequence of the magnetic field being frozen in the electron fluid, the charge neutrality enforcing the total ion density to be the same as the electron density, and the dominance of solar wind ions over PUIs in the total ion density.

4.3 Comparison of Simulated and Observed Magnetic Field Turbulence

Since high-resolution magnetic data (48-second averages) are available from Voyager 2 in the inner heliosheath, we can directly compare the observed turbulent magnetic spectrum with the magnetic spectrum predicted by the three-fluid simulation in frequency domain at a virtual spacecraft flying at the speed of Voyager 2. For this purpose, we selected all the Voyager 2 data from 2009 when the spacecraft was sampling the fully developed turbulent region of the inner heliosheath. Since the typical length of continuous data segments is about 2 to 6 hours per day because of the telemetry constraints of Voyager 2, we limited our data analysis to the frequency range between 10^{-5} Hz and 10^{-2} Hz to avoid artifacts at lower frequencies due to the long data gaps. Missing data were linearly interpolated to a regular grid of 48-second resolution. We applied Welshs averaged periodogram method described in Section 3.2 to compute the average power spectrum of the turbulent magnetic field intensity observed by Voyager 2 in the year 2009. A similar spectrum was computed for the magnetic field time series of the virtual spacecraft flown in the multi-fluid simulation. The simulated and observed magnetic turbulence spectra are presented in Figs. 8a and 8d.

The multi-fluid simulation closely reproduces the observed magnetic turbulence spectrum below the proton gyrofrequency with a scaling exponent of -1.7, which is very close to the Kolmogorov scaling exponent of $-5/3$ in incompressible fluids. However, as it is demonstrated in Fig. 7, the spectral slope of magnetosonic turbulence in frequency domain is not the same as the spectral slope in wave number domain due to the breaking down of Taylors hypothesis in the inner heliosheath. This implies that the observed turbulent magnetic field spectrum is not a classical forward-cascade Kolmogorov spectrum, contrary to Fraternale et al. (2019). The Voyager 2 turbulent magnetic spectrum (Fig. 8c) also shows a narrow peak close to the proton gyrofrequency and its harmonics, which confirms the presence of ion-ion hybrid resonance. Resonance peaks at the gyrofrequencies of α particles and interstellar He^+ PUIs are also present, as predicted by theory. However, these minor ion species were not included in the numerical three-fluid simulation. The observed turbulent magnetic spectrum is known to be affected by noise at frequencies above the proton gyrofrequency (Fraternale et al., 2019). Therefore, we cannot make a reliable comparison between the simulated and observed turbulent magnetic spectra in the high-frequency dissipation range. Nevertheless, both the observed and simulated turbulent magnetic spectra exhibit a spectral break around the proton gyrofrequency, where the 2-D magnetosonic turbulence is forced by the ion-ion hybrid resonance instability.

Overturning downstream propagating LFF and HFF waves produce both forward and reverse shocklets in the fully developed turbulence region of the inner heliosheath. Shocklets appear as sudden jumps in the magnetic field, which is expected to produce outliers in the distribution of magnetic field increments. In order to validate the presence of forward and reverse shocklets in the turbulent inner heliosheath, we computed the distribution functions of magnetic field increments for the 48-second resolution Voyager 2 data. A similar distribution function was computed for the magnetic field time series of the virtual spacecraft in the multi-fluid simulation. The simulated and observed distribution functions of magnetic field increments are presented in Fig. 8b and 8d. The best fitting Gaussian distributions are indicated by the dashed parabola curves. Both

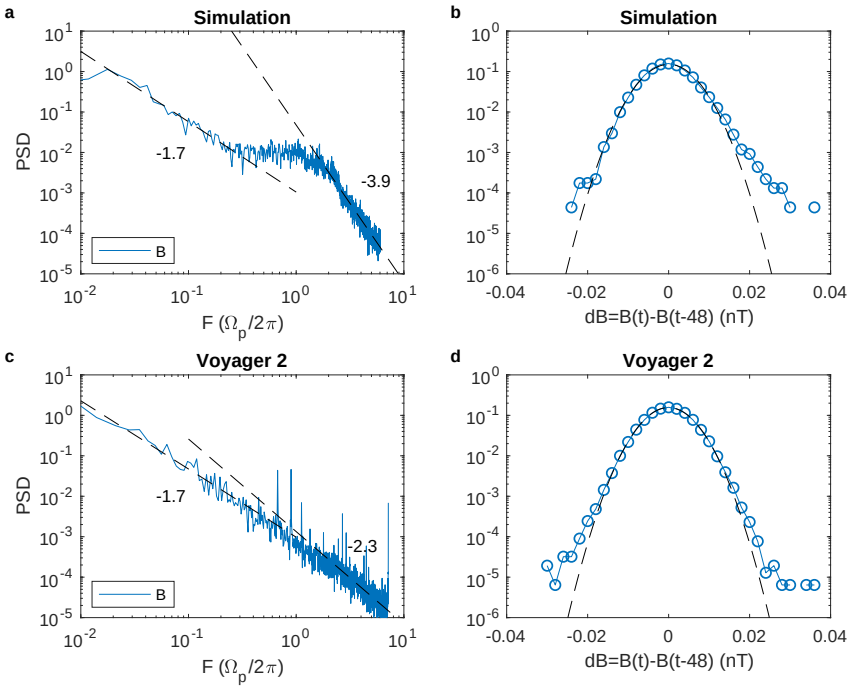

Figure 8. Model validation with Voyager 2 high-resolution magnetic field observations. (a) Simulated magnetic turbulence spectrum in frequency domain and (b) simulated distribution of magnetic field increments as it would be observed by the Voyager 2 spacecraft in the inner heliosheath. (c) Voyager 2 magnetic turbulence spectrum and (d) Voyager 2 distribution of magnetic field increments observed in the inner heliosheath in year 2009. The best fitting spectral slopes are plotted as dashed lines and marked with the corresponding scaling exponents in panels a and c. The best fitting Gaussian distributions are plotted as dashed curves in panels b and c. The three-fluid simulation closely reproduces the observed frequency-domain magnetic turbulence spectrum with a scaling exponent of -1.7 on fluid scale. The simulation also reproduces the observed non-Gaussian distribution of magnetic field increments in the inner heliosheath.

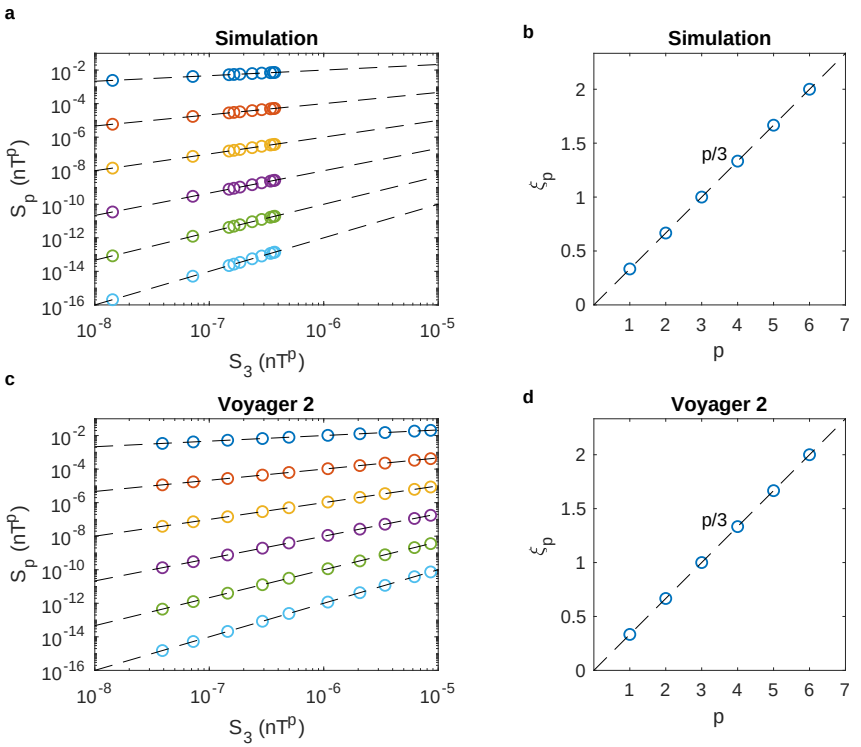

Figure 9. Kolmogorov-Kraichnan scaling of fast magnetosonic turbulence in the inner heliosheath. (a) Scaling of simulated magnetic field structure functions as a function of the third-order moment. (b) Scaling exponents of the structure functions in panel a as a function of the order p. (c) Scaling of Voyager 2 magnetic field structure functions observed in the inner heliosheath in year 2009 as a function of the third-order moment. (d) Scaling exponents of the structure functions in panel c as a function of the order p. The best linear fits are plotted as dashed lines in panels a and c. The predicted $p/3$ scaling of the scaling exponents are plotted as dashed lines in panels b and d. The three-fluid simulation reproduces the observed Kolmogorov-Kraichnan scaling of compressible turbulence in the inner heliosheath.

the observed and simulated distribution functions show significant deviations from Gaussian. The wings of the distributions at large positive and negative increments, which can be approximated with a symmetric Tsallis distribution at different scales (Burlaga & Ness, 2009), correspond to forward and reverse magnetosonic shocklets propagating downstream in the spacecraft frame. The similar shapes of the observed and simulated distribution functions confirm the presence of magnetosonic shocklets in the heliosheath and further validate the shock driven magnetosonic turbulence model.

In order to analyze the multi-scale properties of fast magnetosonic turbulence in the inner heliosheath, we computed the structure functions of the magnetic field for the simulated time series of the virtual spacecraft flown at the speed of Voyager 2 across the fully developed turbulence region of the multi-fluid simulation. As a comparison, we computed the magnetic structure functions at Voyager 2 in the inner heliosheath in year 2009. We used only the existing data points in this analysis without interpolating over the data gaps. The magnetic structure function is defined as

$$S_p(\tau) = \langle |B(t) - B(t+\tau)|^p \rangle \,, \tag{20}$$

where p is the order of the structure function, τ is the difference in time, and the angle brackets mean the expected value. The structure functions were evaluated up to the 6th order at the smallest scales with τ ranging from 48 s to 6 hours. At larger scales the Voyager 2 magnetic structure functions are strongly affected by the data gaps. Kraichnans theory of 2-D turbulence predicts that the structure functions do not scale close to the production range where the turbulence is forced. However, the structure functions should scale as a function of the third-order moment, and the scaling exponents should be $p/3$, which is referred to as Kolmogorov-Kraichnan scaling.

We plotted the magnetic structure functions as a function of the third-order moment in Figs. 9a and 9c for the simulated and observed compressible turbulence, respectively. The structure functions perfectly scale as a function of the third-order moment. The dashed lines represent the best linear fits, and the slopes of the best fitting lines provide a scaling exponent (ξ_p) for each structure function. These scaling exponents are plotted as a function of p in Figs. 9b and 9d for the simulated and observed turbulence, respectively. The scaling exponents of the structure functions (ξ_p) follow the theoretically predicted Kolmogorov-Kraichnan scaling, indicated as a dashed line in Figs. 9b and 9d, with the scaling exponent of $p/3$ for both the simulated and observed compressible turbulence. The Kolmogorov-Kraichnan scaling is equivalent to the self-similarity of the turbulence at different scales. This can be proven as follows. The Kolmogorov-Kraichnan scaling states that

$$\log S_4 = \frac{4}{3}\log S_3 + c_1, \tag{21}$$

$$\log S_2 = \frac{2}{3}\log S_3 + c_2, \tag{22}$$

where c_1 and c_2 are constants. From Eqs. (21) and (22) we get

$$\log S_4 = 2\log S_2 + c_3, \tag{23}$$

where c_3 is constant. This means that S_4/S_2^2 is constant, which is the definition of self-similarity in turbulence theory. Thus, we have shown that the 2-D fast magnetosonic turbulence in the inner heliosheath is self-similar at different scales.

5 Conclusions

We have shown that the dispersion of fast magnetosonic waves in the non-equilibrium solar wind plasma plays an important role in the energy dissipation downstream of the TS. Due to the hot pickup ions, the TS is a subcritical quasi-stationary dispersive shock wave consisting of a foot, a ramp and an extended oscillatory region downstream of the shock front. The non-stationary nature of the dispersive shock wave provides a constant source of downstream propagating fast magnetosonic perturbations even in case of steady upstream solar wind conditions. Downstream propagating nonlinear fast magnetosonic waves grow until they reach a maximum amplitude and overturn, starting to propagate backward in the frame of the downstream propagating wave. The counterpropagating fast magnetosonic waves result in forward and reverse shocklets that maintain self-consistent quasi-stationary compressible turbulence in the inner heliosheath. The nonlinear growth of magnetosonic waves is driven by the ion-ion hybrid resonance instability of solar wind ions and PUIs. The 2-D compressible turbulence in the inner heliosheath shows a double cascade where energy is transferred to large scales and enstrophy is transferred to small scales as predicted by Kraichnans theory. The inverse energy cascade eventually heats and accelerates the solar wind plasma at the large wavelength limit. The numerical three-fluid simulation of the TS and the inner heliosheath has been validated with

high-resolution magnetic field observations by Voyager 2. The magnetic turbulence spectrum observed by Voyager 2 is closely reproduced by the simulation in frequency domain below the proton gyrofrequency. However, it has been shown that Taylors hypothesis breaks down in the inner heliosheath. Consequently, the observed magnetic turbulence spectrum is not a Kolmogorov spectrum in wave number domain. The observed non-Gaussian distribution of magnetic field increments has been explained with shocklets produced by nonlinearly steepened fast magnetosonic waves. Last but not least, the multi-scale analysis of magnetic field variations revealed a self-similar compressible turbulence on ion scales close to the production range where the turbulence is forced by ion-ion hybrid resonance in agreement with Kraichnans theory of 2-D turbulence and Voyager 2 observations in the inner heliosheath. In this study we simulated the TS in a one-dimensional domain with constant upstream solar wind conditions. Further work is needed to explore the non-stationary nature of the TS in 2-dimensional geometry, with turbulent upstream solar wind driving, and more realistic ion composition that includes solar He^{++} ions as well as interstellar He^{+} PUIs. These minor ion species are expected to introduce additional fast magnetosonic modes as well as additional ion-ion resonance peaks in the turbulent magnetic spectrum.

Acknowledgments

B.Z. was mainly supported by NASA under Grant No. 80NSSC18K1214. The authors were partially supported by NASA DRIVE Grant No. 80NSSC20K0603, Our Heliospheric Shield. V.F. was partially supported by NASA grant No. 80NSSC18K1209. The 48 s resolution Voyager 2 magnetic field data are accessible at https://vgrmag.gsfc.nasa.gov/data.html.

References

Balogh, A., & Treumann, R. A. (2013). Physics of collisionless shocks. New York: Springer. doi: 10.1007/978-1-4614-6099-2

Biskamp, D. (1973, October). Collisionless shock waves in plasmas. Nucl. Fusion, 13, 719-740. doi: 10.1088/0029-5515/13/5/010

Burlaga, L. F., & Ness, N. F. (2009, September). Compressible "Turbulence" Observed in the Heliosheath by Voyager 2. Astrophys. J., 703(1), 311-324. doi: 10.1088/0004-637X/703/1/311

Burlaga, L. F., Ness, N. F., Acuña, M. H., Lepping, R. P., Connerney, J. E. P., & Richardson, J. D. (2008, July). Magnetic fields at the solar wind termination shock. Nature, 454(7200), 75-77. doi: 10.1038/nature07029

Burlaga, L. F., Ness, N. F., & Acuna, M. H. (2007, July). Linear magnetic holes in a unipolar region of the heliosheath observed by Voyager 1. J. Geophys. Res., 112(A7), A07106. doi: 10.1029/2007JA012292

Burlaga, L. F., Ness, N. F., Richardson, J. D., Decker, R. B., & Krimigis, S. M. (2016, February). Heliosheath Magnetic Field and Plasma Observed by Voyager 2 during 2012 in the Rising Phase of Solar Cycle 24. Astrophys. J., 818(2), 147. doi: 10.3847/0004-637X/818/2/147

Chalov, S. V., & Fahr, H. J. (2013, June). The role of solar wind electrons at the solar wind termination shock. Month. Not. Royal Astron. Soc., 433, L40-L43. doi: 10.1093/mnrasl/slt052

Chashei, I. V., & Fahr, H. J. (2014, April). On Solar-Wind Electron Heating at Large Solar Distances. Sol. Phys., 289(4), 1359-1370. doi: 10.1007/s11207-013-0403-8

Coroniti, F. V. (1970, May). Dissipation discontinuities in hydromagnetic shock waves. J. Plasma Phys., 4(2), 265-282. doi: 10.1017/S0022377800004992

Dubinin, E. M., Sauer, K., & McKenzie, J. F. (2006, November). Nonlinear 1-D stationary flows in multi-ion plasmas - sonic and critical loci - solitary and "oscillatory" waves. Ann. Geophys., 24(11), 3041-3057. doi:

10.5194/angeo-24-3041-2006

Edmiston, J. P., & Kennel, C. F. (1984, December). A parametric survey of the first critical Mach number for a fast MHD shock. J. Plasma Phys., 32(3), 429-441. doi: 10.1017/S002237780000218X

Fahr, H. J., Chashei, I. V., & Verscharen, D. (2014, November). Traveling solar-wind bulk-velocity fluctuations and their effects on electron heating in the heliosphere. Astron. Astrophys., 571, A78. doi: 10.1051/0004-6361/201424421

Fahr, H.-J., Sylla, A., Fichtner, H., & Scherer, K. (2016, September). On the evolution of the κ distribution of protons in the inner heliosheath. J. Geophys. Res., 121(9), 8203-8214. doi: 10.1002/2016JA022561

Fraternale, F., Pogorelov, N. V., Richardson, J. D., & Tordella, D. (2019, February). Magnetic Turbulence Spectra and Intermittency in the Heliosheath and in the Local Interstellar Medium. Astrophys. J., 872(1), 40. doi: 10.3847/1538-4357/aafd30

Glocer, A., Tóth, G., Ma, Y., Gombosi, T., Zhang, J. C., & Kistler, L. M. (2009, December). Multifluid Block-Adaptive-Tree Solar wind Roe-type Upwind Scheme: Magnetospheric composition and dynamics during geomagnetic storms—Initial results. J. Geophys. Res., 114(A12), A12203. doi: 10.1029/2009JA014418

Hoefer, M. A. (2014, June). Shock Waves in Dispersive Eulerian Fluids. J. Nonlin. Sci., 24(3), 525-577. doi: 10.1007/s00332-014-9199-4

Isenberg, P. A. (1986, September). Interaction of the solar wind with interstellar neutral hydrogen: three-fluid model. J. Geophys. Res., 91(A9), 9965-9972. doi: 10.1029/JA091iA09p09965

Kraichnan, R. H. (1967, July). Inertial Ranges in Two-Dimensional Turbulence. Physics of Fluids, 10(7), 1417-1423. doi: 10.1063/1.1762301

McComas, D. J., Zirnstein, E. J., Bzowski, M., Elliott, H. A., Randol, B., Schwadron, N. A., ... Weaver, H. (2017, November). Interstellar Pickup Ion Observations to 38 au. Astrophys. J. Suppl. Ser., 233(1), 8. doi: 10.3847/1538-4365/aa91d2

McKenzie, J. F., Marsch, E., Baumgaertel, K., & Sauer, K. (1993, May). Wave and stability properties of multi-ion plasmas with applications to winds and flows. Ann. Geophys., 11(5), 341-353.

Opher, M., Loeb, A., Drake, J., & Toth, G. (2020, March). A small and round heliosphere suggested by magnetohydrodynamic modelling of pick-up ions. Nature Astron.. doi: 10.1038/s41550-020-1036-0

Randol, B. M., McComas, D. J., & Schwadron, N. A. (2013, May). Interstellar Pick-up Ions Observed between 11 and 22 AU by New Horizons. Astrophys. J., 768(2), 120. doi: 10.1088/0004-637X/768/2/120

Richardson, J. D., Kasper, J. C., Wang, C., Belcher, J. W., & Lazarus, A. J. (2008, July). Cool heliosheath plasma and deceleration of the upstream solar wind at the termination shock. Nature, 454(7200), 63-66. doi: 10.1038/nature07024

Scherer, K., Jörg Fahr, H., Fichtner, H., Sylla, A., Richardson, J. D., & Lazar, M. (2018, January). Uncertainties in the heliosheath ion temperatures. Ann. Geophys., 36(1), 37-46. doi: 10.5194/angeo-36-37-2018

Stone, E. C., Cummings, A. C., McDonald, F. B., Heikkila, B. C., Lal, N., & Webber, W. R. (2005, September). Voyager 1 Explores the Termination Shock Region and the Heliosheath Beyond. Science, 309(5743), 2017-2020. doi: 10.1126/science.1117684

Stone, E. C., Cummings, A. C., McDonald, F. B., Heikkila, B. C., Lal, N., & Webber, W. R. (2008, July). An asymmetric solar wind termination shock. Nature, 454(7200), 71-74. doi: 10.1038/nature07022

Taylor, G. I. (1938, February). The Spectrum of Turbulence. Proc. Royal Soc. London, 164(919), 476-490. doi: 10.1098/rspa.1938.0032

Toida, M., & Aota, Y. (2013, August). Finite beta effects on low- and high-

frequency magnetosonic waves in a two-ion-species plasma. Physics of Plasmas, 20(8), 082301. doi: 10.1063/1.4817169

Usmanov, A. V., & Goldstein, M. L. (2006, July). A three-dimensional MHD solar wind model with pickup protons. J. Geophys. Res., 111(A7), A07101. doi: 10.1029/2005JA011533

Usmanov, A. V., Goldstein, M. L., & Matthaeus, W. H. (2014, June). Three-fluid, Three-dimensional Magnetohydrodynamic Solar Wind Model with Eddy Viscosity and Turbulent Resistivity. Astrophys. J., 788(1), 43. doi: 10.1088/0004-637X/788/1/43

Whang, Y. C. (1998, August). Solar wind in the distant heliosphere. J. Geophys. Res., 103(A8), 17419-17428. doi: 10.1029/98JA01524

Yang, Z., Liu, Y. D., Richardson, J. D., Lu, Q., Huang, C., & Wang, R. (2015, August). Impact of Pickup Ions on the Shock Front Nonstationarity and Energy Dissipation of the Heliospheric Termination Shock: Two-dimensional Full Particle Simulations and Comparison with Voyager 2 Observations. Astrophys. J., 809(1), 28. doi: 10.1088/0004-637X/809/1/28

Zank, G. P., Heerikhuisen, J., Pogorelov, N. V., Burrows, R., & McComas, D. (2010, January). Microstructure of the Heliospheric Termination Shock: Implications for Energetic Neutral Atom Observations. Astrophys. J., 708(2), 1092-1106. doi: 10.1088/0004-637X/708/2/1092

Zank, G. P., Hunana, P., Mostafavi, P., & Goldstein, M. L. (2014, December). Pickup Ion Mediated Plasmas. I. Basic Model and Linear Waves in the Solar Wind and Local Interstellar Medium. Astrophys. J., 797(2), 87. doi: 10.1088/0004-637X/797/2/87

Zieger, B., Opher, M., Schwadron, N. A., McComas, D. J., & Tóth, G. (2013, June). A slow bow shock ahead of the heliosphere. Geophys. Res. Lett., 40(12), 2923-2928. doi: 10.1002/grl.50576

Zieger, B., Opher, M., Tóth, G., Decker, R. B., & Richardson, J. D. (2015, September). Constraining the pickup ion abundance and temperature through the multifluid reconstruction of the Voyager 2 termination shock crossing. J. Geophys. Res., 120(9), 7130-7153. doi: 10.1002/2015JA021437

Figure 1.

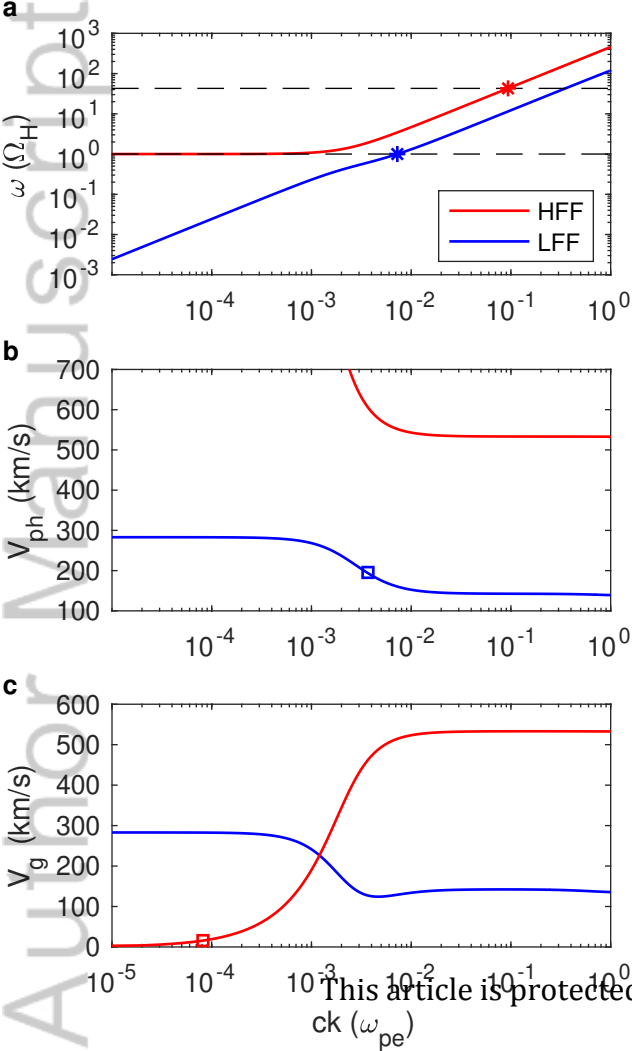

Figure 2.

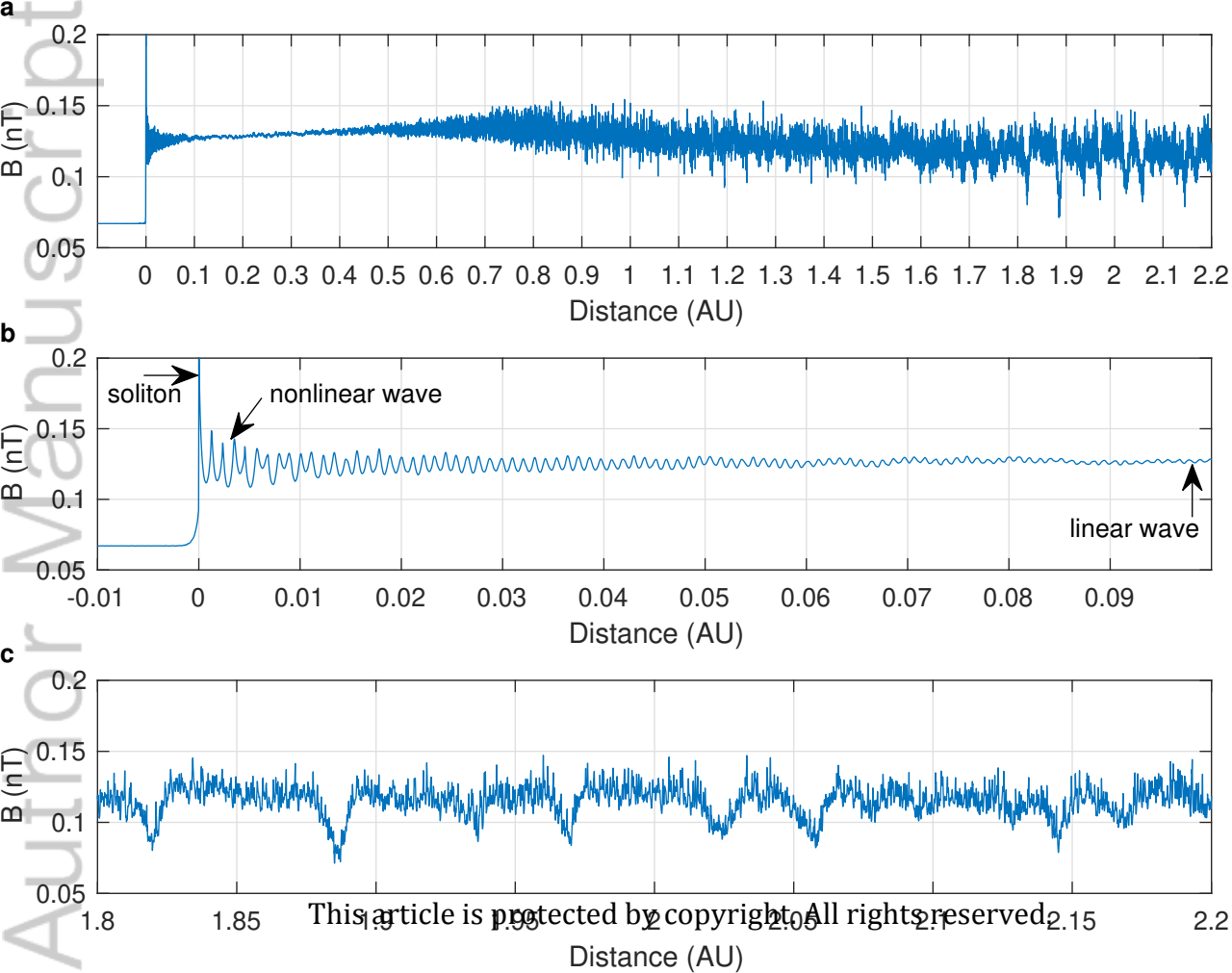

Figure 3.

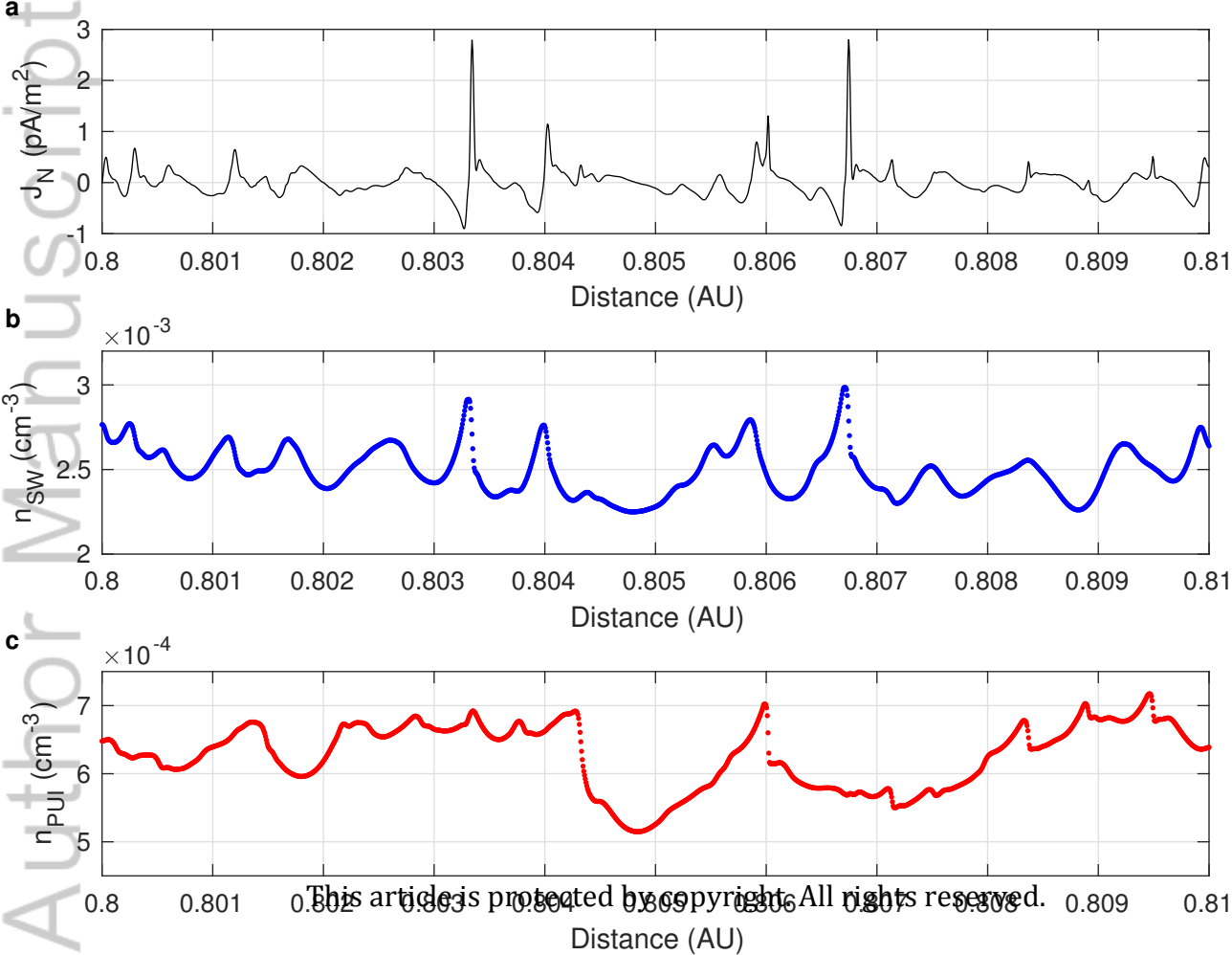

Figure 4.

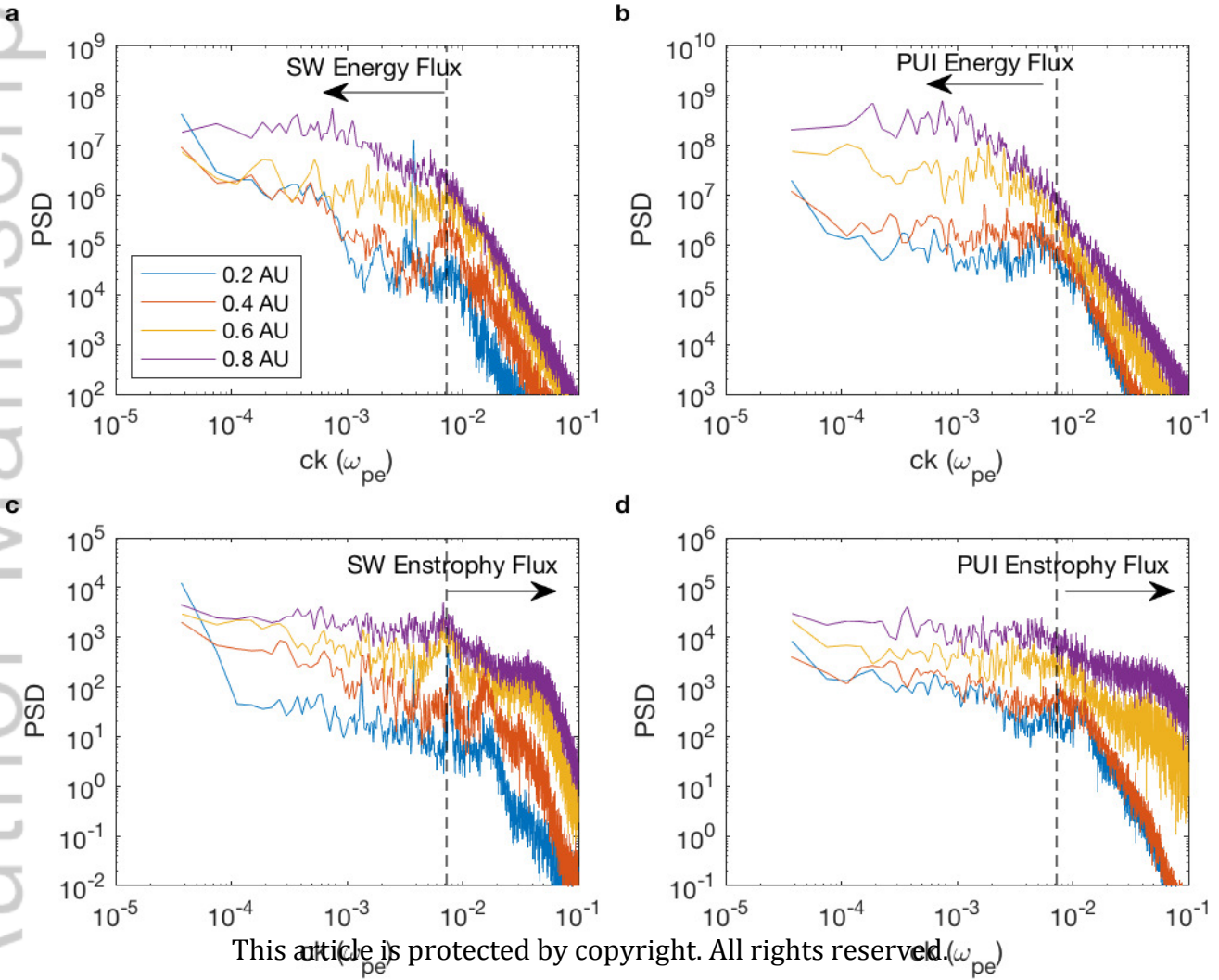

Figure 5.

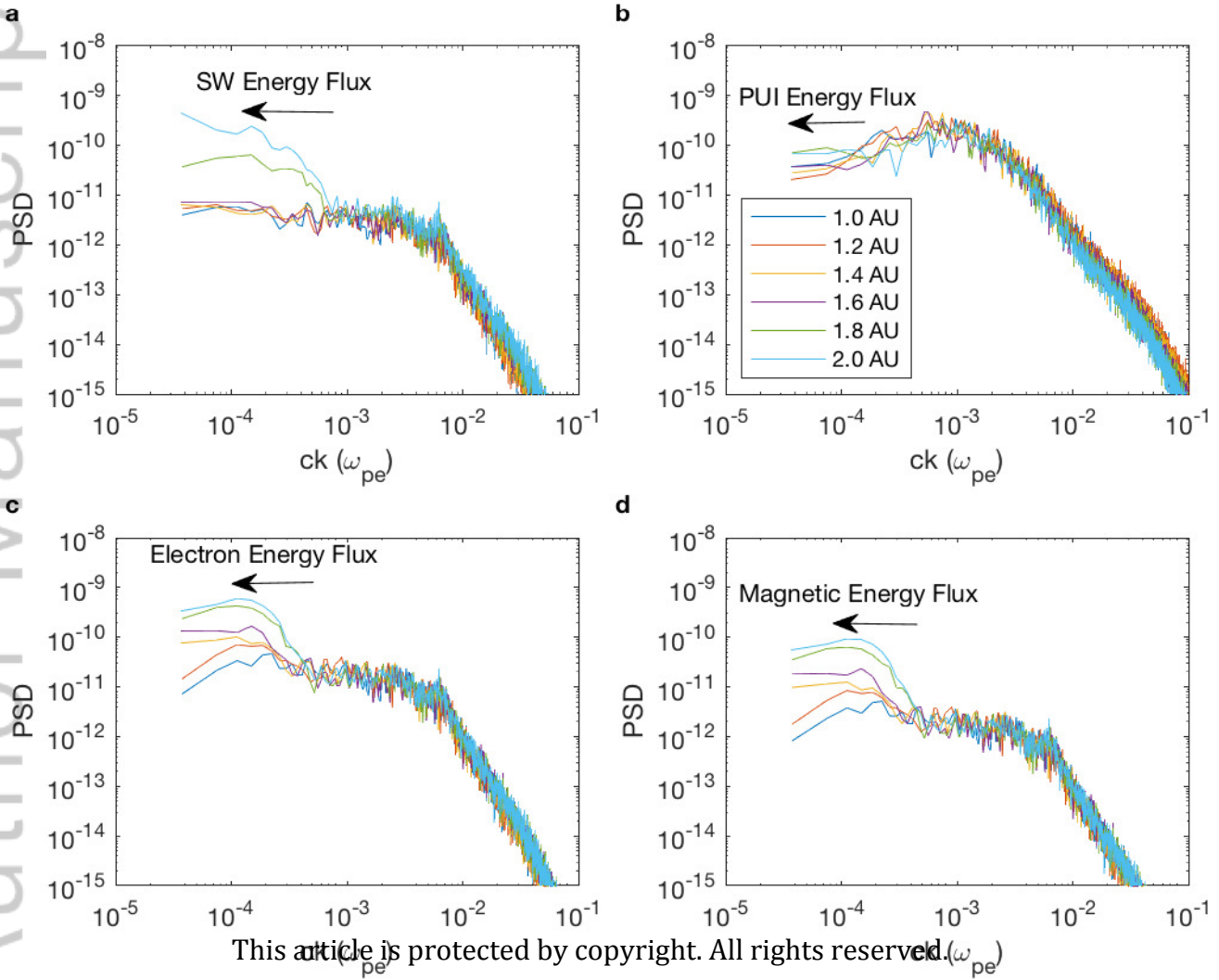

Figure 6.

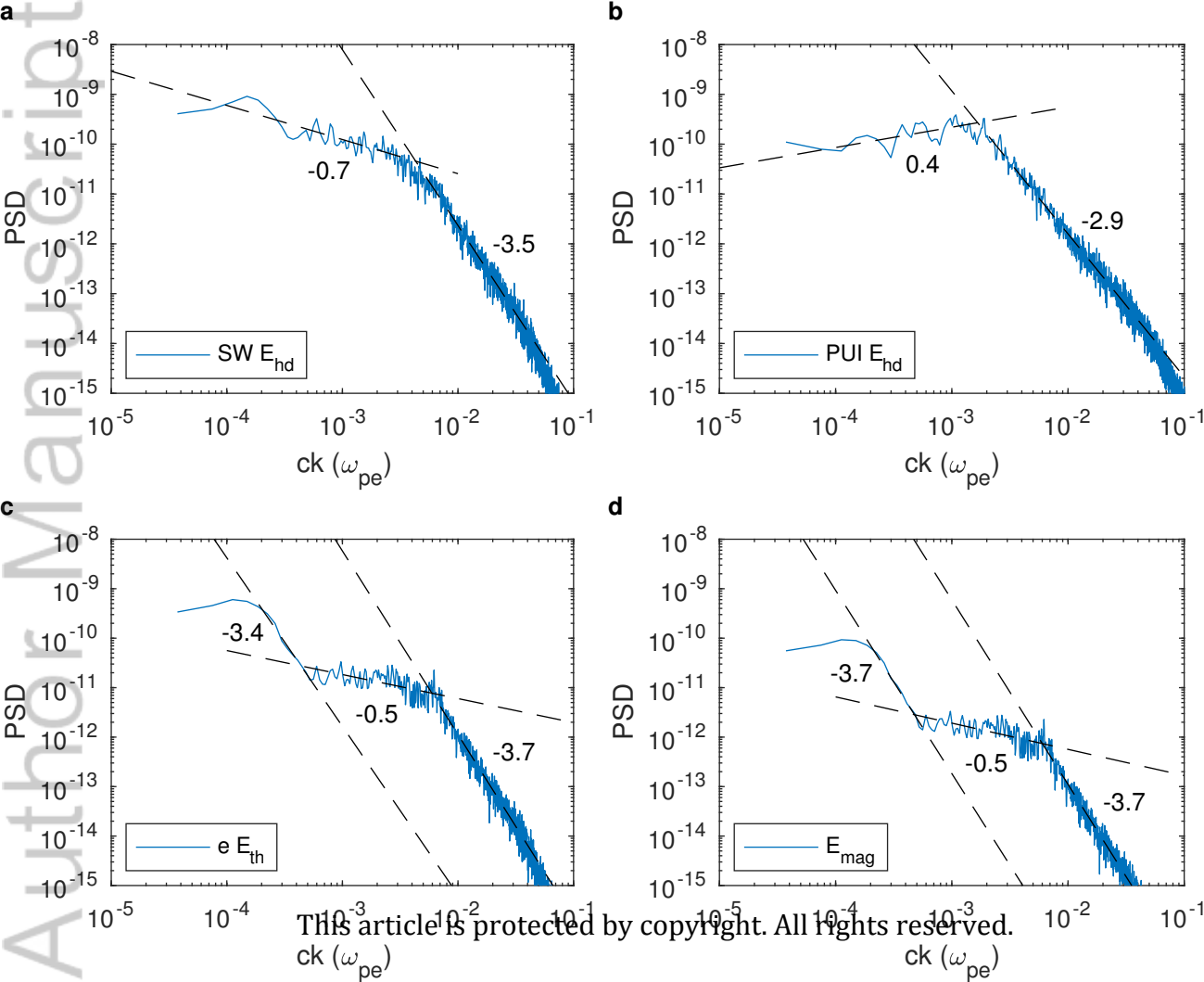

Figure 7.

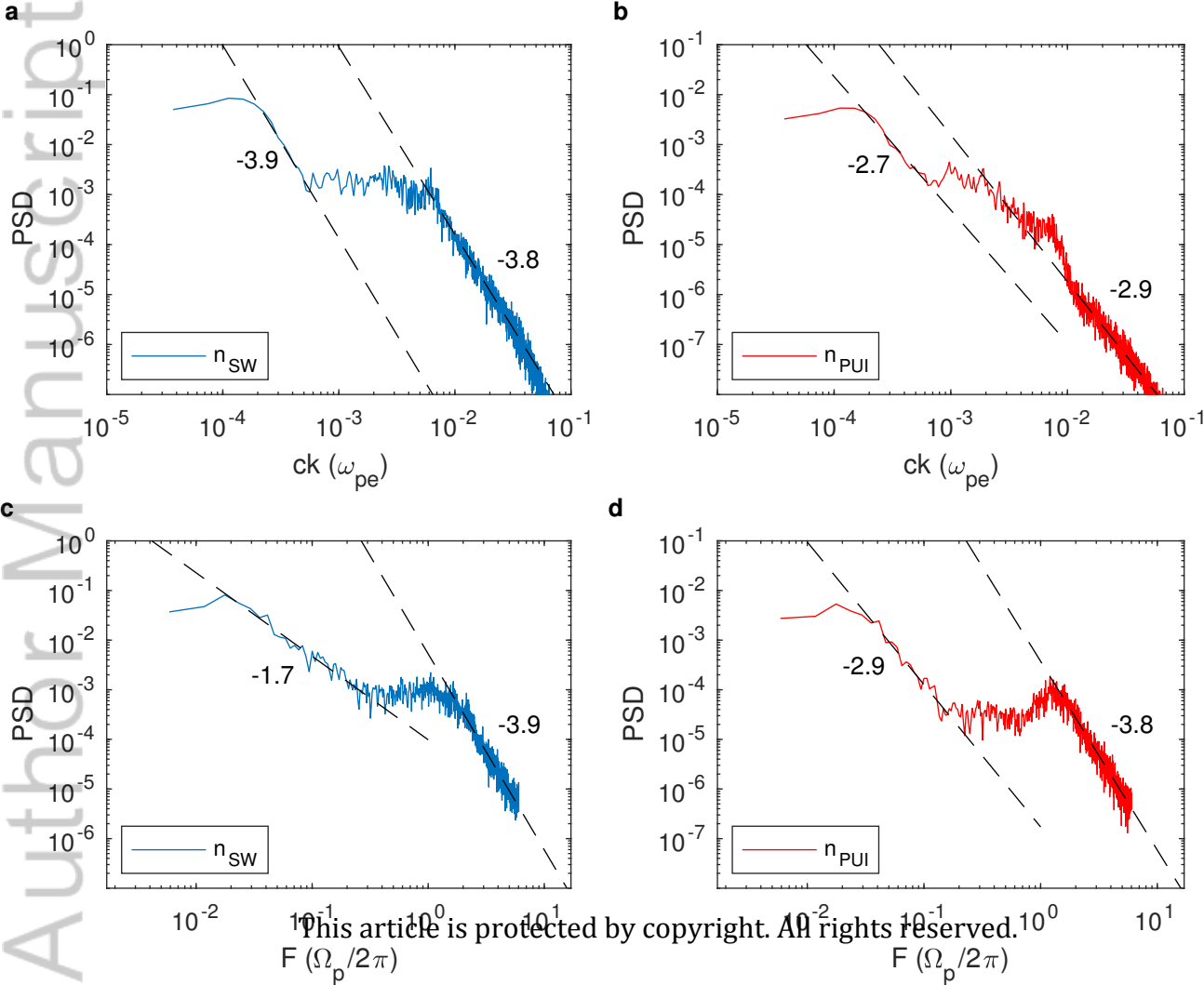

Figure 8.

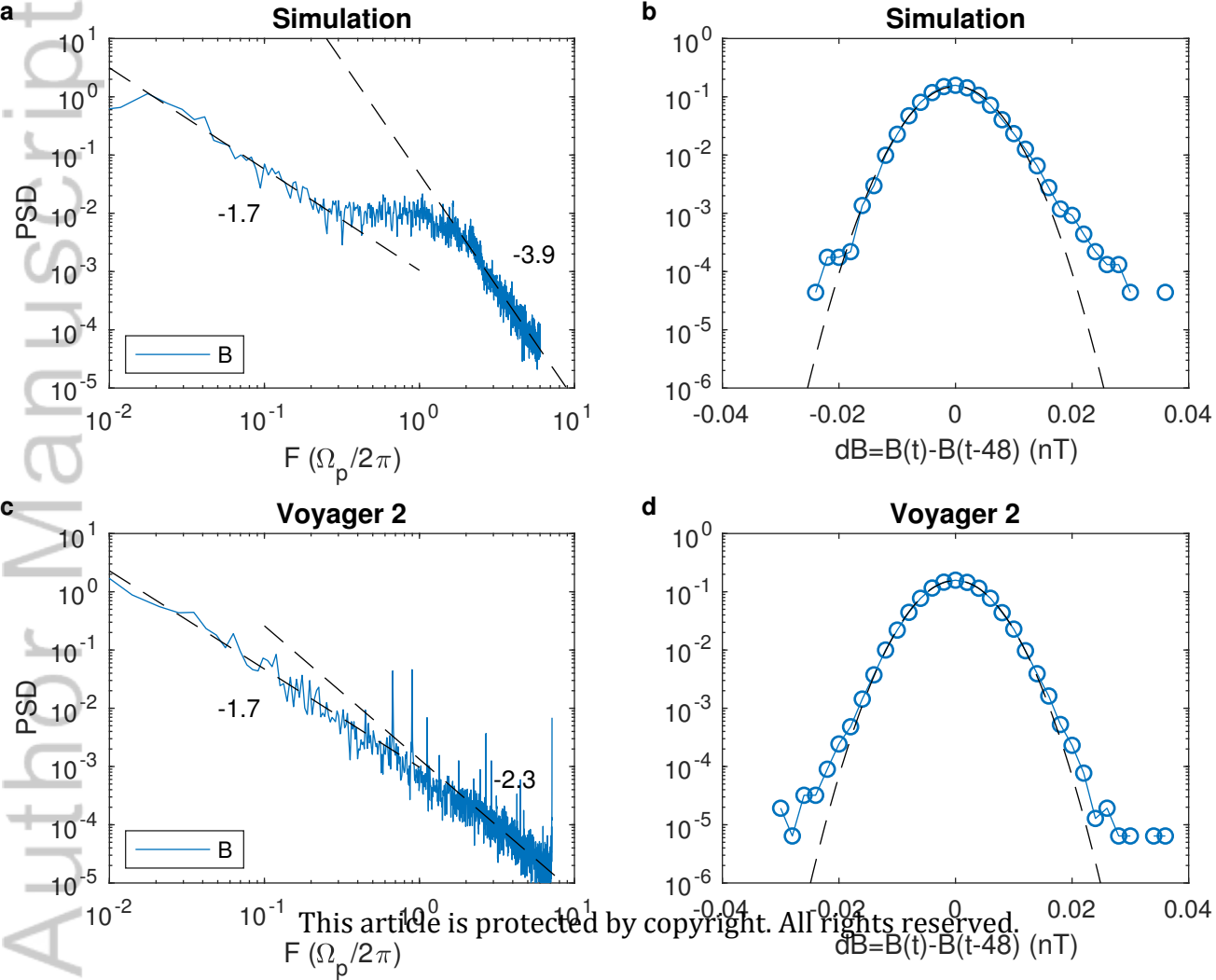

Figure 9.

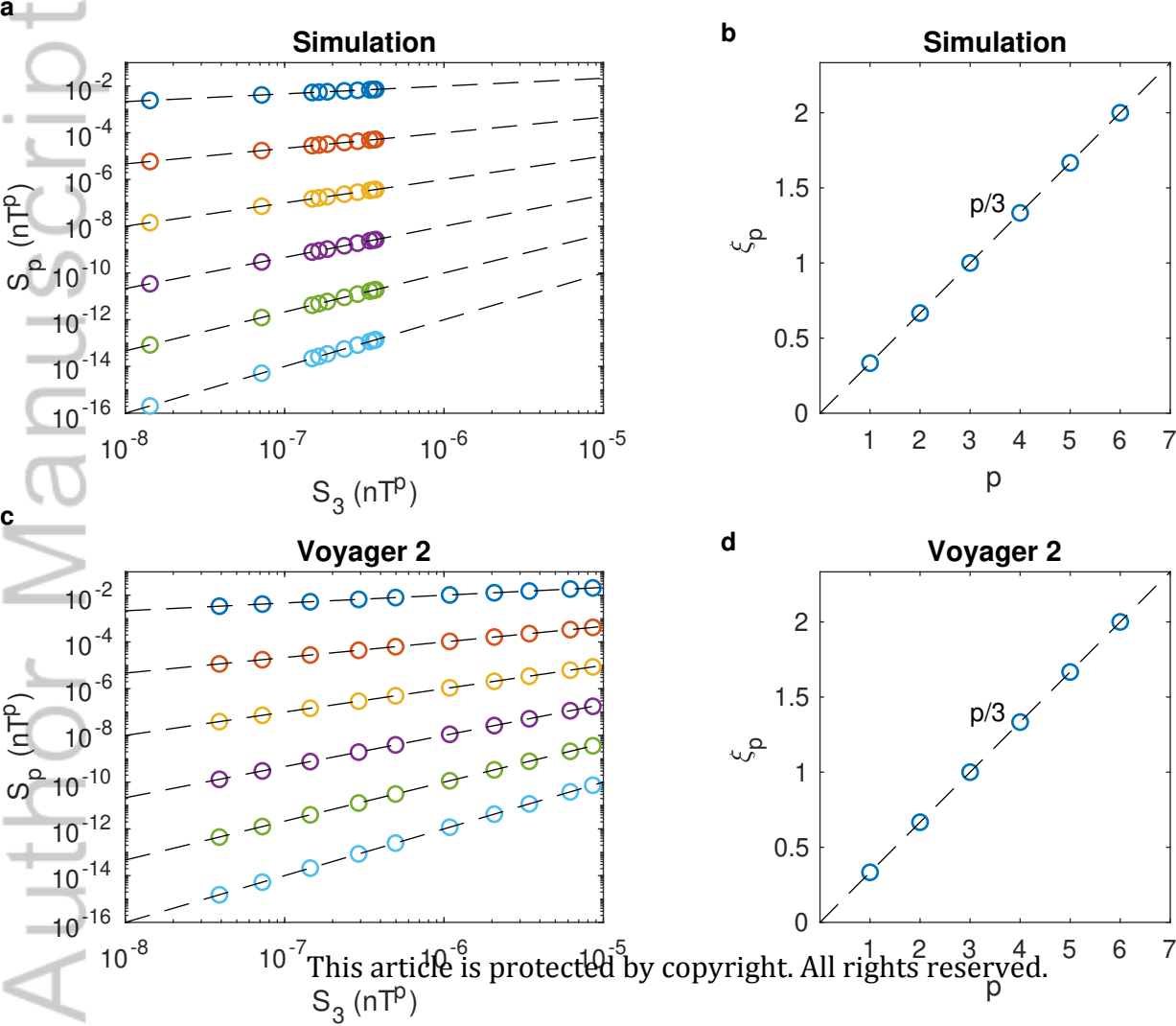

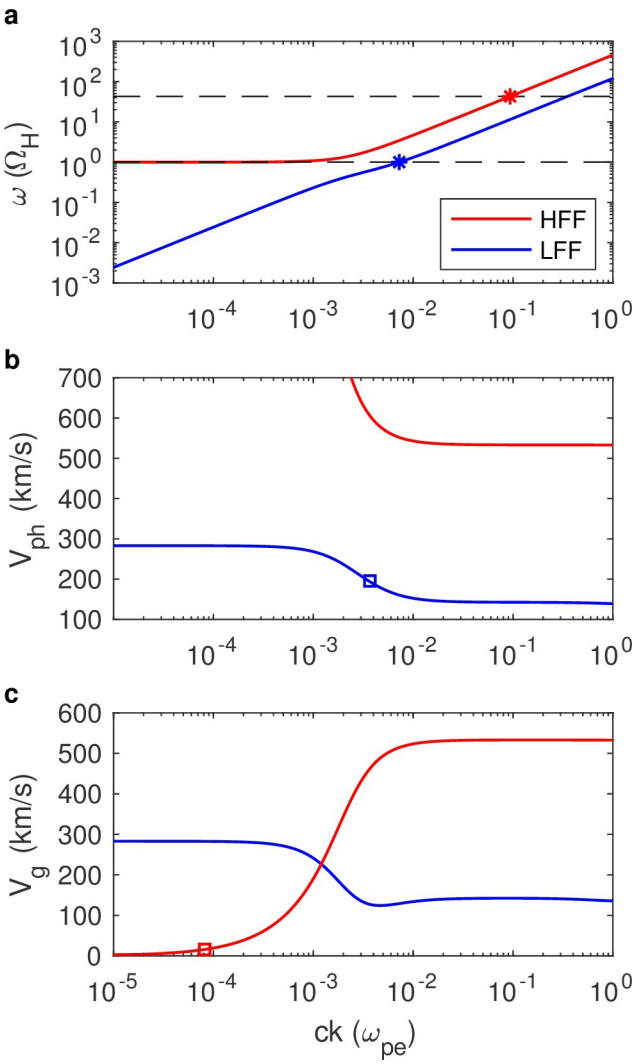

jgra_56004_2020ja028393-f01-z-.eps

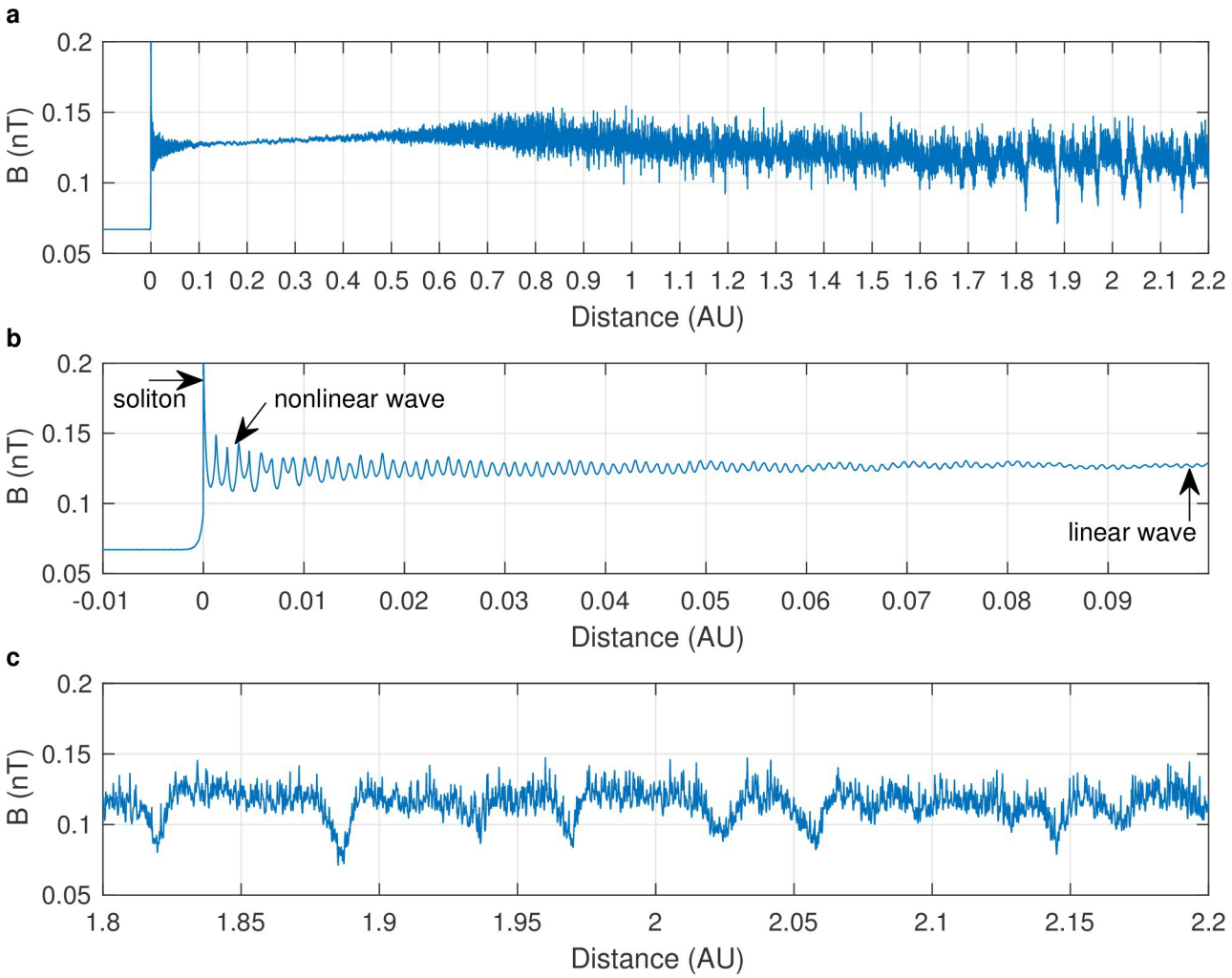

jgra_56004_2020ja028393-f02-z-.eps

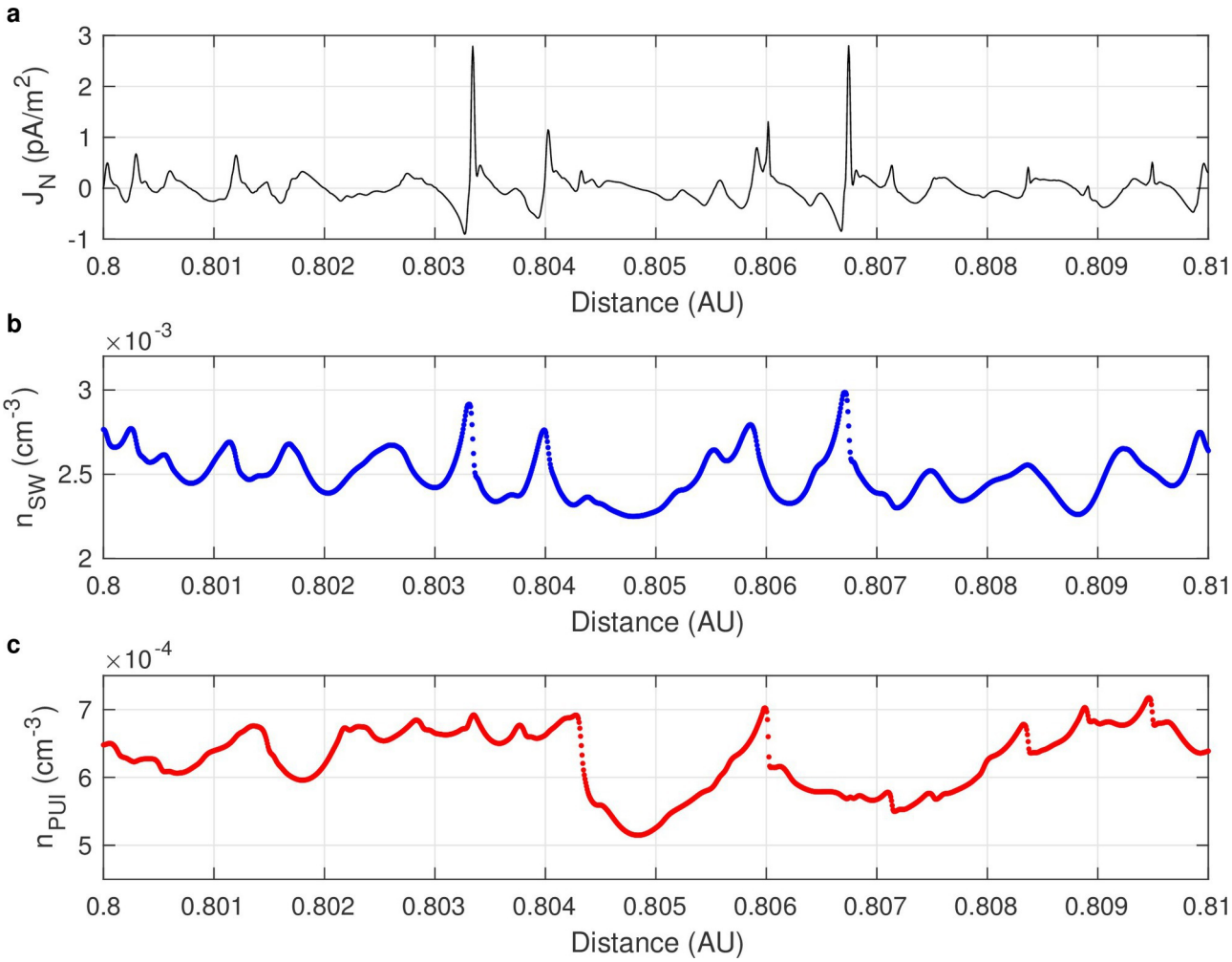

jgra_56004_2020ja028393-f03-z-.eps

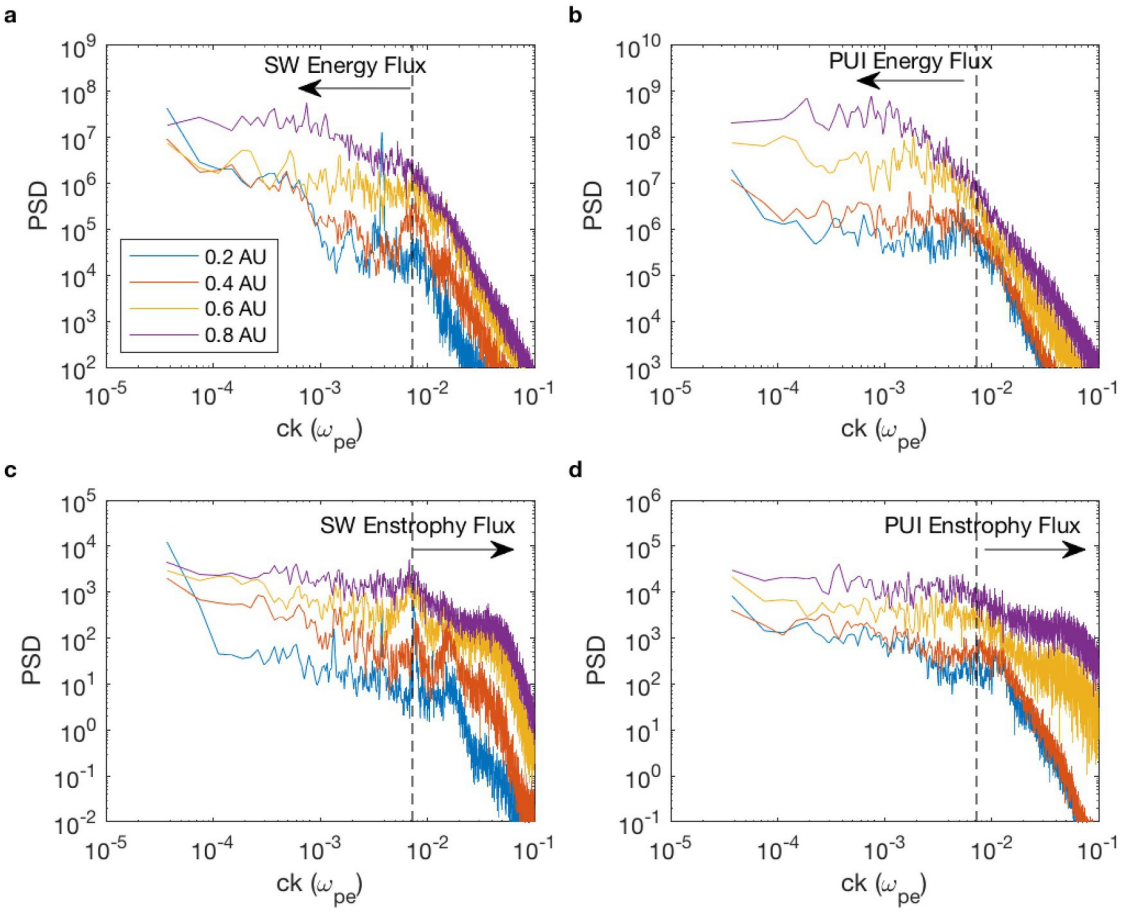

jgra_56004_2020ja028393-f04-z-.eps

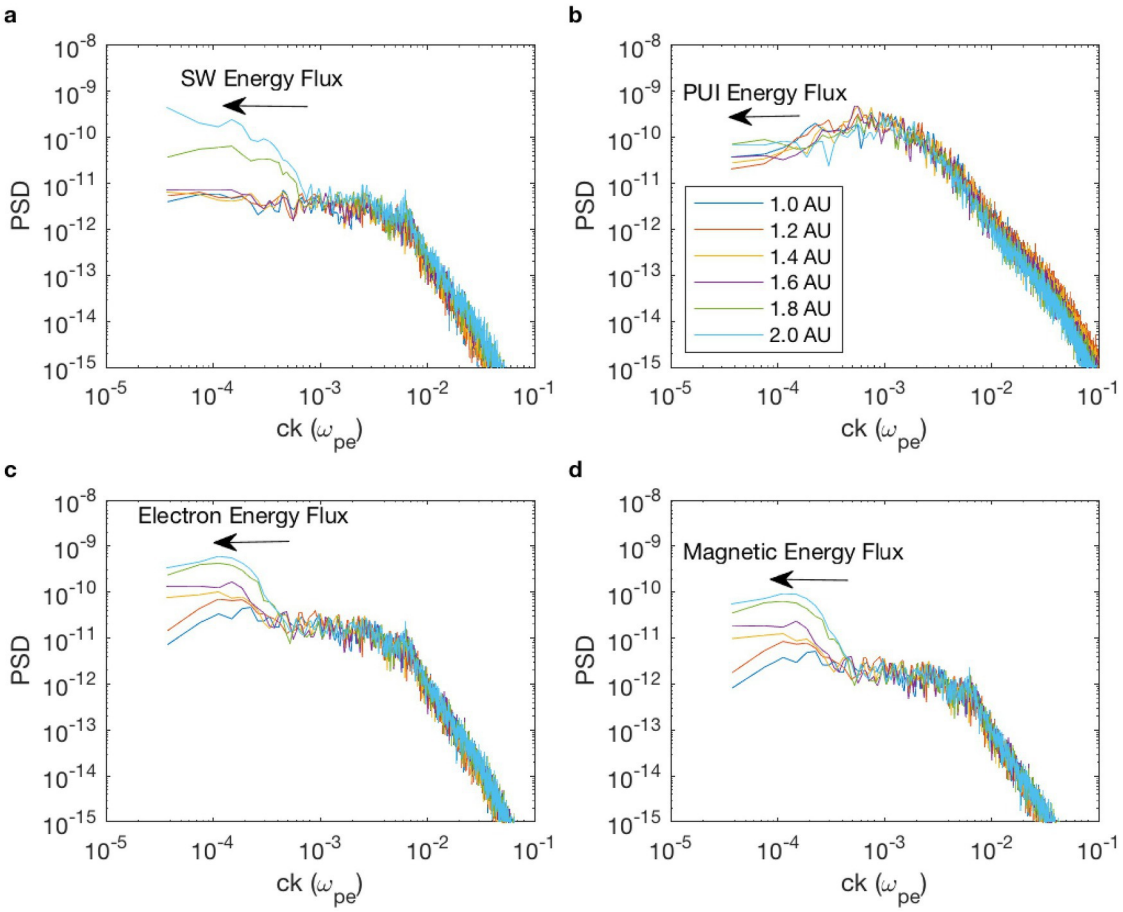

jgra_56004_2020ja028393-f05-z-.eps

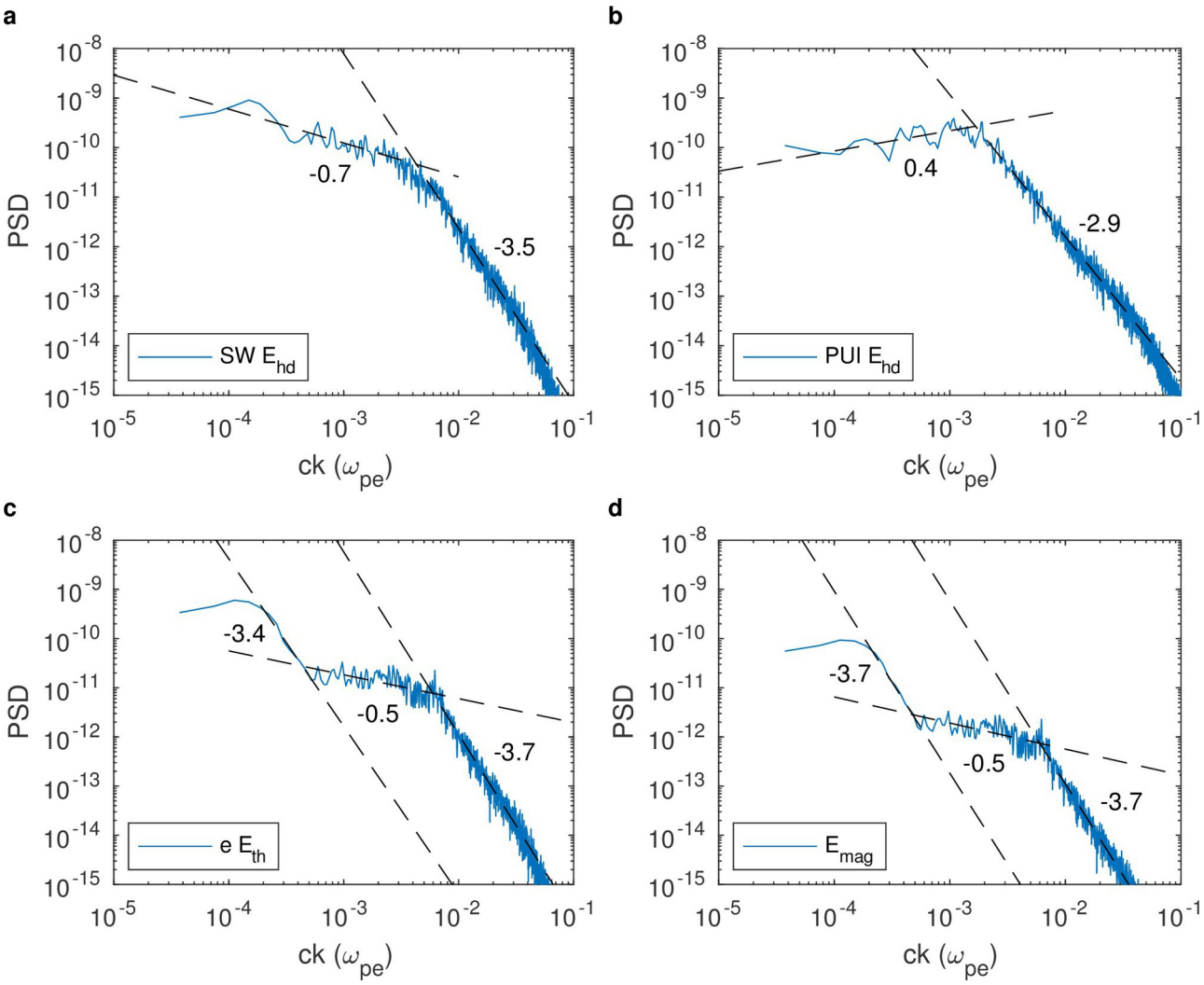

jgra_56004_2020ja028393-f06-z-.eps

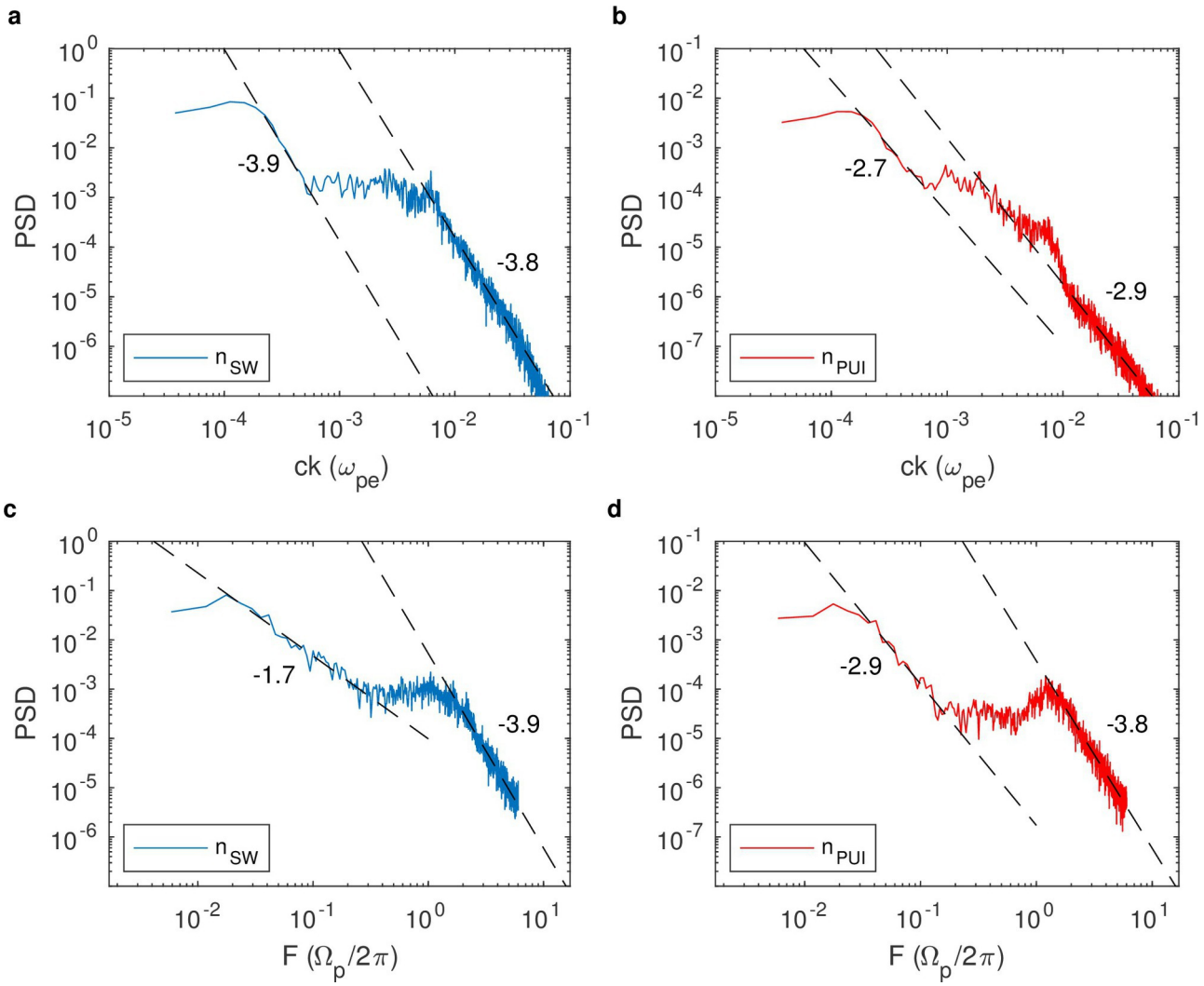

jgra_56004_2020ja028393-f07-z-.eps

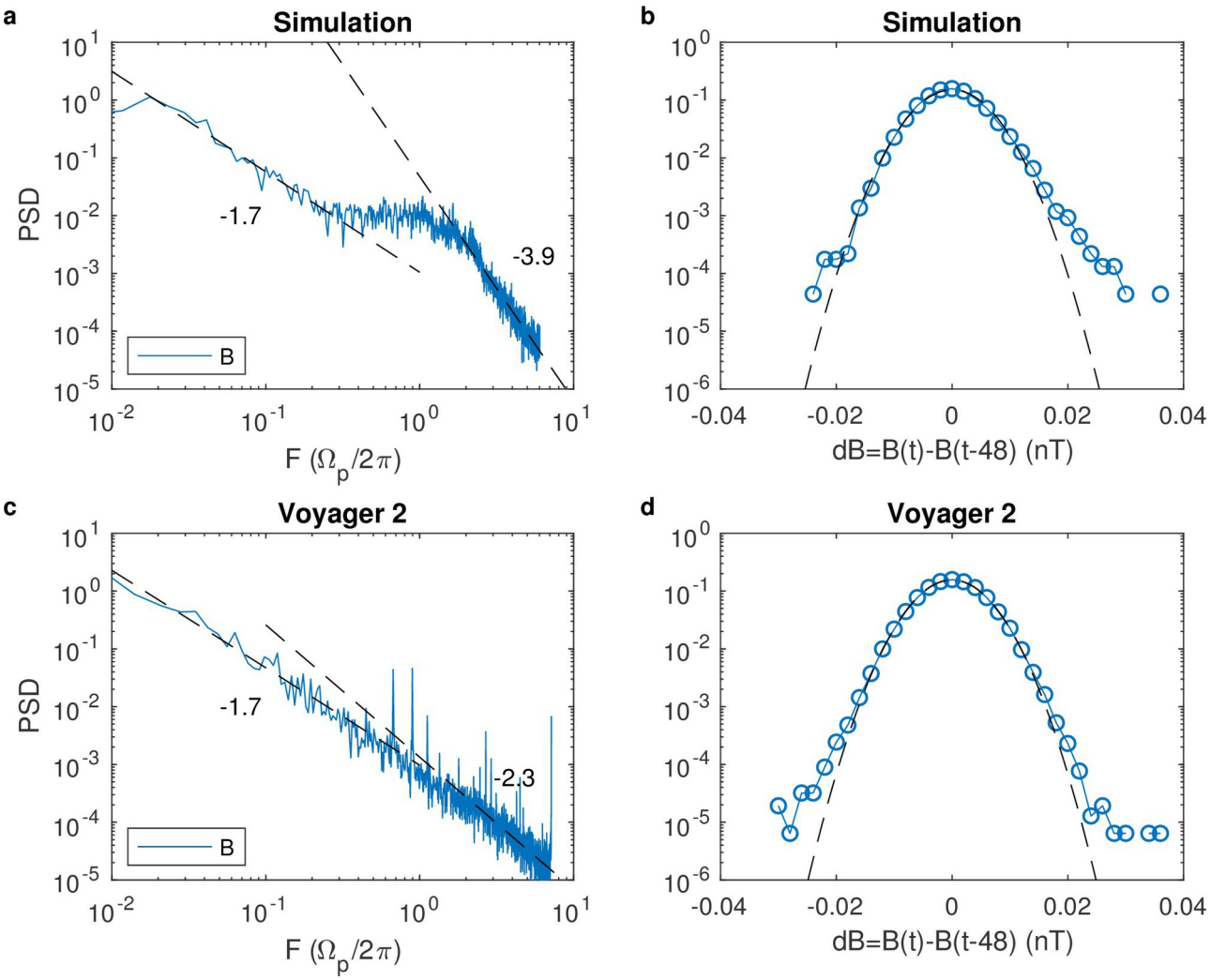

jgra_56004_2020ja028393-f08-z-.eps

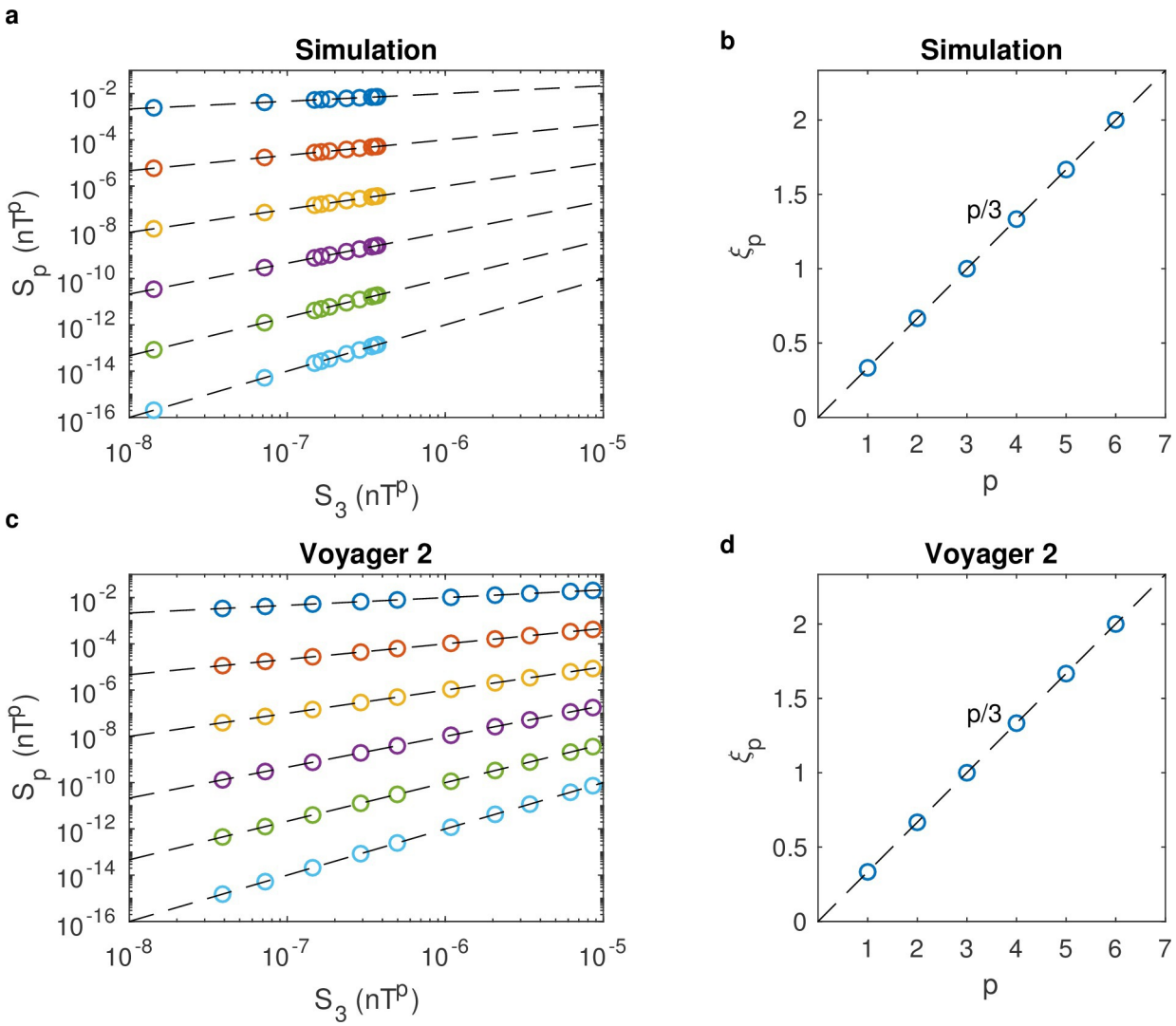

jgra_56004_2020ja028393-f09-z-.eps